Space Sci Rev (2013) 179:337–381
DOI 10.1007/s11214-012-9950-9

The Relativistic Electron-Proton Telescope (REPT) Instrument on Board the Radiation Belt Storm Probes (RBSP) Spacecraft: Characterization of Earth's Radiation Belt High-Energy Particle Populations

D.N. Baker · S.G. Kanekal · V.C. Hoxie · S. Batiste · M. Bolton · X. Li · S.R. Elkington · S. Monk · R. Reukauf · S. Steg · J. Westfall · C. Belting · B. Bolton · D. Braun · B. Cervelli · K. Hubbell · M. Kien · S. Knappmiller · S. Wade · B. Lamprecht · K. Stevens · J. Wallace · A. Yehle · H.E. Spence · R. Friedel

Received: 12 April 2012 / Accepted: 9 October 2012 / Published online: 14 December 2012

Abstract Particle acceleration and loss in the million electron Volt (MeV) energy range (and above) is the least understood aspect of radiation belt science. In order to measure cleanly and separately both the energetic electron and energetic proton components, there is a need for a carefully designed detector system. The Relativistic Electron-Proton Telescope (REPT) on board the Radiation Belt Storm Probe (RBSP) pair of spacecraft consists of a stack of high-performance silicon solid-state detectors in a telescope configuration, a collimation aperture, and a thick case surrounding the detector stack to shield the sensors from penetrating radiation and bremsstrahlung. The instrument points perpendicular to the spin axis of the spacecraft and measures high-energy electrons (up to ∼20 MeV) with excellent sensitivity and also measures magnetospheric and solar protons to energies well above

D.N. Baker (✉) · V.C. Hoxie · S. Batiste · M. Bolton · X. Li · S.R. Elkington · S. Monk · R. Reukauf · S. Steg · J. Westfall · C. Belting · D. Braun · B. Cervelli · K. Hubbell · M. Kien · S. Knappmiller · S. Wade · B. Lamprecht · J. Wallace · A. Yehle
Laboratory for Atmospheric and Space Physics, 3665 Discovery Drive, Boulder, CO 80303-7820, USA
e-mail: daniel.baker@lasp.colorado.edu

S.G. Kanekal
Goddard Space Flight Center, Greenbelt, MD 20771, USA

B. Bolton
Ball Aerospace, 1600 Commerce Street, Boulder, CO 80301, USA

K. Stevens
Efficient Logic Designs, 2260 Floral Drive, Boulder, CO 80304, USA

H.E. Spence
Center for Earth, Oceans, and Space, University of New Hampshire, Durham, NH 03824, USA

R. Friedel
Los Alamos National Laboratory, PO Box 1663, Los Alamos, NM 87545, USA

$E = 100$ MeV. The instrument has a large geometric factor ($g = 0.2$ cm^2 sr) to get reasonable count rates (above background) at the higher energies and yet will not saturate at the lower energy ranges. There must be fast enough electronics to avert undue dead-time limitations and chance coincidence effects. The key goal for the REPT design is to measure the directional electron intensities (in the range 10^{-2}–10^6 particles/cm^2 s sr MeV) and energy spectra ($\Delta E/E \sim 25$ %) throughout the slot and outer radiation belt region. Present simulations and detailed laboratory calibrations show that an excellent design has been attained for the RBSP needs. We describe the engineering design, operational approaches, science objectives, and planned data products for REPT.

Keywords Radiation detection · Particle sensors · Radiation belts · Space weather

1 Introduction

The existence of Earth's radiation belts was established in 1958 by James A. Van Allen and co-workers using a simple Geiger counter system on board the Explorer 1 and Explorer 3 spacecraft missions. Since that time, many NASA satellites, combined with observations from other space-based platforms, have provided insight into the phenomenology and range of processes active in the Van Allen belts. A watershed event occurred in 1990–1991 when CRRES (Combined Radiation and Release Effects Satellite) was placed in a near-equatorial, geosynchronous transfer orbit with the express purpose of understanding the effects of the space radiation environment (Johnson and Kierein 1992). CRRES was well instrumented for understanding the nature of the energetic particles and fields in the inner magnetosphere, and observations from CRRES suggested a range of processes acting in the Van Allen belts that obviously were not well understood at that time.

As shown in Fig. 1, researchers were surprised when on Orbit 588 (24 March 1991), there suddenly (on time scales <1 min) appeared very high fluxes of trapped electrons extending in energy up to at least 15 MeV. A solar-driven shock wave had impacted the Earth's magnetosphere and had suddenly produced a new radiation belt deep within the pre-existing confines of the terrestrial magnetic field. This was a pivotal moment in radiation belt science (Blake et al. 1992). The results obtained from the CRRES mission were limited by the single-point nature of the measurements and by the ~10-hour orbital period which did not allow the spacecraft to view the global evolution of the belts on shorter time scales. Unfortunately, CRRES was lost 14 months into a planned 3-year mission as a result of a battery failure.

Apart from CRRES observations in its geostationary transfer orbit, continuous long-term monitoring of the energetic particle environment at geosynchronous orbit (geocentric radial distant $r = 6.6R_E$) has been accomplished over many years via the NOAA Geostationary Orbit Environmental Satellite (GOES) series of spacecraft (http://www.oso.noaa.gov/goesstatus), as well as through particle detectors on board other geostationary orbit spacecraft (e.g., Baker et al. 1981) instrumented by Los Alamos National Laboratory (LANL). The measurements available from these platforms on the fringes of the outer radiation belt have typically offered only limited energy and time resolution, allowing partial inferences about the evolving energy spectrum and spatial extent of the belts. However, neither the GOES nor the LANL spacecraft measure the electric fields driving particle energization in the magnetosphere, and neither set of platforms is capable of providing information about the radiation environment at radial distances $<6.6R_E$.

Inside geosynchronous orbit, the available measurements near the magnetic equator have been very sparse. Measurements are available from some of the spacecraft comprising the

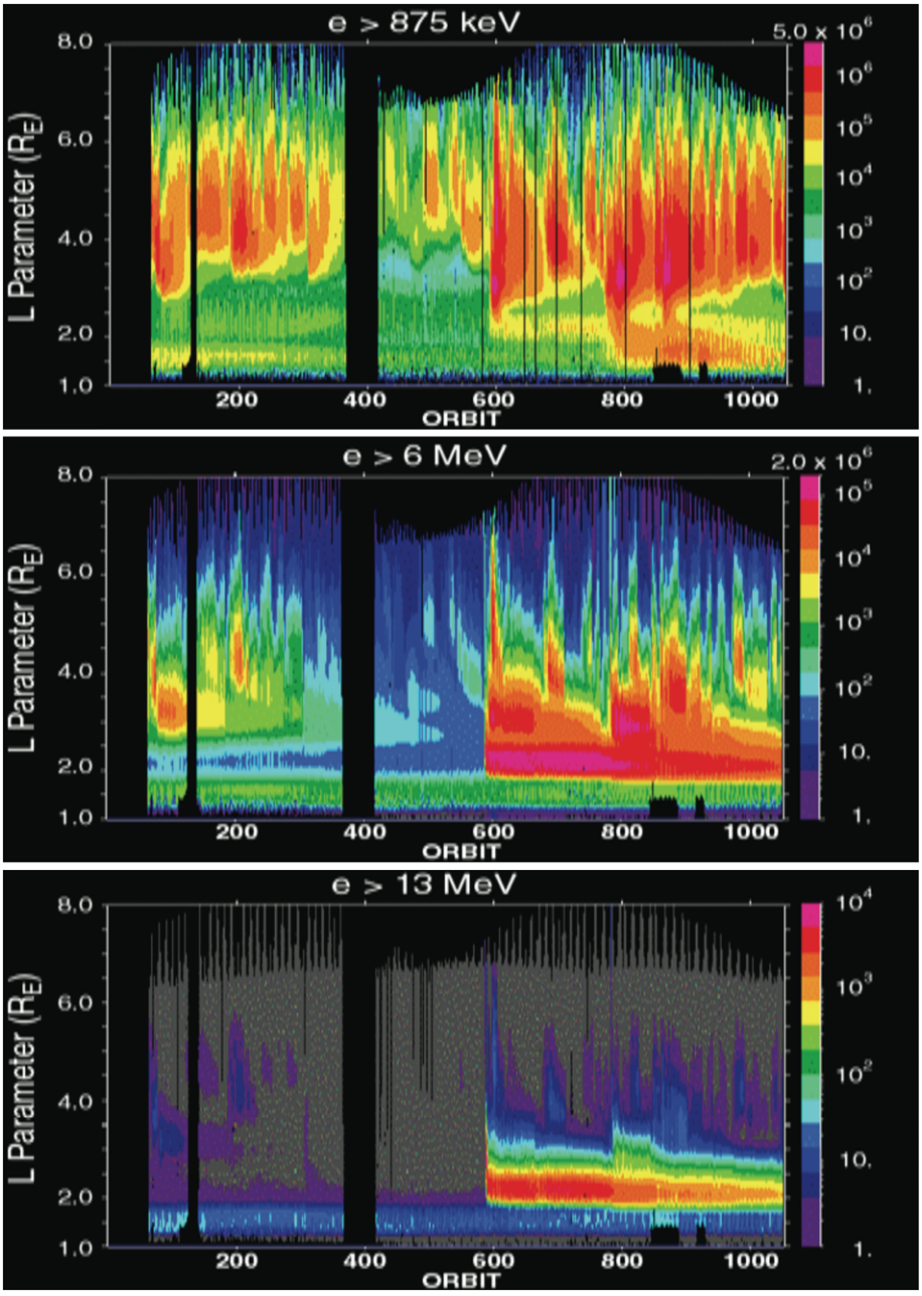

Fig. 1 Summary of the energetic electron flux through the 15 months of the CRRES mission as a function of L-Shell for (*top panel*) >875 keV, (*middle panel*) >6 MeV, and (*bottom panel*) >13 MeV (Blake et al. 1992). Note the very large increase near orbit 588 (24 March 1991), especially at the highest energies

Global Positioning System (GPS) constellation which lie in highly inclined orbits at $4.2 R_E$ radial distance. However, the instruments on these satellites are generally simple and lack high-energy or pitch-angle resolution. On the other hand, key measurements of radiation belt properties have been made since 1992 by the Solar, Anomalous, and Magnetospheric Particle Explorer (SAMPEX) spacecraft (Baker et al. 1993). SAMPEX continues at present to make measurements at low altitudes (∼600 km), but is quite far away from the equatorial acceleration region. The NOAA/POES (Polar-Orbiting Environmental Satellite System) also has made long-term radiation belt measurements in low-Earth orbit. The NASA spacecraft POLAR (1996–2007) carried both electric and magnetic field instruments (Acuña et al. 1996) and was capable of energy-resolved particle measurements at relativistic energies. However, it was placed in a polar orbit that generally only allowed observation of particle populations with relatively small equatorial pitch angles. And, similar to CRRES, the utility of POLAR observations of the radiation belts was limited by the single-point nature of the observations and also its relatively long (∼18-hour) orbital period.

Based on this brief survey of observing platforms, it is evident that there is a clear need for new, comprehensive radiation belt observations from low-inclination satellites. In this paper we describe an innovative high-energy, high-precision particle detection system called the Relativistic Electron-Proton Telescope (REPT). This new sensor system on board the Radiation Belt Storm Probes (RBSP) spacecraft pair will provide crucial new data to help resolve long-standing radiation belt science questions.

2 Requirements and Expected Results

2.1 Science Motivation

REPT will make the measurements necessary to gain fundamental new understanding of the relative importance of different physical acceleration and loss processes that are hypothesized to shape the radiation belt particle populations. REPT provides the basic measurements at a range of altitudes necessary for the development of the next-generation radiation belt specification models. Thus REPT will be an essential component in addressing the science goals of the RBSP mission (see Mauk et al. 2012 and Spence et al. 2012). The instruments will also help monitor the total radiation dose, and will help assess single event upset and deep-dielectric charging of electronic components on-orbit.

While the superstorm of March 1991 mentioned previously provided a striking example of prompt acceleration and deep injection leading to the formation of a new radiation belt, such events are not the norm. Moreover, CRRES happened to be fortuitously located to observe this event. More usual are the smaller storm-related injection events that occur several times per year (Lorentzen et al. 2002). The dual RBSP spacecraft mission will increase the radial visit frequency by 50 % over what CRRES achieved, correspondingly increasing the likely radial range of coverage that may be obtained during a prompt injection of energetic particles.

In contrast to the powerful superstorm acceleration as described above, the response of outer zone electron flux to solar wind variation more typically occurs over a timescale of hours to days (Baker et al. 1998). Increases in flux at higher energies is correlated with increased solar wind speed and southward interplanetary magnetic field (IMF). The former may drive the growth of velocity-shear instability along the magnetopause (in analogy with the way that wind drives surface waves on water). The southward IMF drives up geomagnetic activity, such as substorms, which can provide the seed population for radiation

belt electrons. Low-frequency, long-wavelength perturbations of the magnetopause boundary can transfer energy to ULF (Ultra-Low Frequency) wave modes within the magnetosphere, with periods up to tens of minutes. Enhancement of wave power at these frequencies has been seen both with ground-based and space-borne magnetic field measurements. REPT, in conjunction with the other RBSP particle measurements, will provide key particle observations of these events covering precisely the needed energy ranges.

The REPT instruments will be able to provide information that clearly tests competing models of particle acceleration, and will highlight where and when they are most important. Measurements suggest that the phase space density of $E > 2$ MeV electrons at geosynchronous orbit can be greater than the phase space density of corresponding electrons with the same first adiabatic invariant at greater distances, contrary to the expectations from radial diffusion models (Li et al. 2001a). Magnetopause motion may contribute to this discrepancy. Another possible explanation is that resonant interactions with whistler waves can energize these electrons. In this scenario, electrons are accelerated from several hundred keV to several MeV over periods of hours through multiple interactions with the whistlers (Roth et al. 1999; Horne and Thorne 1998).

Whistler-mode chorus emission excited during enhanced convective injection of plasma sheet electrons into the inner magnetosphere may transfer energy between the suprathermal (tens of keV) and relativistic populations (Horne et al. 2005a, 2005b). The rate of acceleration is strongly dependent on plasma density, specifically, the ratio between the electron gyrofrequency and the plasma frequency. Chorus is primarily excited in the low-density region during enhanced convection events, and has the highest probability of occurrence on the dawnside beyond the plasmapause (Meredith et al. 2003). Using realistic VLF (Very Low Frequency) wave properties, Horne et al. (2005a, 2005b) have shown that the flux of outer zone MeV electrons at $L = 4.5$ can be enhanced by more than a factor of ten during the 1–2 day recovery phase of a storm. During the acceleration, the energy spectrum and pitch-angle distributions of resonant electrons are predicted to evolve in a unique way (Horne et al. 2003). REPT measurements of pitch angle and spectral evolution during the energization will help characterize thisenergization process.

Paulikas and Blake (1979) and Baker et al. (1979, 1990) showed that MeV electrons often appear near geostationary orbit with a delay of about 2 days after the passage of fast solar wind streams. It is now believed these recurring acceleration events may be associated with strong turbulent Alfvenic wave fields in the fast streams. Correlation of electron flux with solar wind velocity fluctuations suggests that dynamic pressure buffeting of the magnetosphere or shear flow instabilities are an important driving force for radial diffusion. A correlation with intense southward IMF over extended periods of time, especially deeper in the magnetosphere ($L \sim 4$), suggests (indirectly) that a necessary condition for strong radial diffusion is the enhancement in large-scale convection electric field or more precisely its fluctuation level. If radial diffusion operates, we must determine what in the magnetosphere or in the solar wind generates the fluctuations that give rise to radial diffusion. In-situ measurements of electric and magnetic fields and particles in the inner magnetosphere, together with upstream solar wind conditions, will enable an assessment of the efficacy and timing of radial diffusion and convection.

The RBSP spacecraft with measurements of electric and magnetic fields, energetic electrons and ions, and plasma density at *spatially separated* points will provide insights into the importance of acceleration mechanisms under different solar wind conditions and at different radial positions inside the magnetosphere. Spacecraft at two separated radial positions will be able to monitor continuously the evolution of the energetic particle spectra and phase space distributions as the acceleration process progresses. Additional prompt acceleration processes due to substorm injection and medium-to-strong interplanetary shocks will

be continuously monitored and easily distinguished from the slower stochastic processes. Information on the azimuthal structure and wave-coherence lengths critical to understanding the radial diffusion problem will be obtained through comparisons between the two RBSP spacecraft, comparisons with the GOES magnetic field measurements at $6.6R_E$ and comparisons to mid-latitude ground magnetometers. Finally, in order to see the "acceleration in action", it is important to have energetic particle measurements on a time scale of about 1–20 seconds since the driving waves have frequencies which vary over periods of 1 minute to 1 hour. Similar requirements obtain for the measurement of energetic particles during shock and substorm induced acceleration. RBSP with REPT will provide this key information.

Determining the rate of loss of radiation belt particles, and the processes responsible for this loss, is also a key component of understanding the overall dynamics of the radiation belts. Fundamental to these efforts is the global measurement of wave activity, particle pitch angle distributions, and global magnetic fields (see Kletzing et al. 2012; Wygant et al. 2012). The dual RBSP mission will significantly enhance the coverage available, allowing observation of wave and particle distributions in local times outside those seen in a single orbit. This is particularly important in the case of scattering through interaction with VLF waves, since the waves involved are expected to be highly localized and may often occur in regions outside the narrow local time region observable from a single orbit. RBSP will increase the instantaneous coverage in radial distance. This will provide crucial information about the radial distribution of the particle losses in the REPT range and suggest the extent to which magnetopause shadowing may be important.

The RBSP mission will provide very important monitoring from MEO (Middle Earth Orbit) altitudes, the data forming a critical input into the development of the next generation radiation belt specification models that will replace AE-8 and AP-8 (see Vette 1991). This work requires coverage of medium energy plasma particles (surface charging), as well as high-energy electrons (>1 MeV; total dose and deep-dielectric charging) and very high-energy protons (>20 MeV) for single event upsets (SEU). Industry has identified the energy bands and orbital requirements as well as the radiation levels and their variability, especially worse case over a variety of integration intervals. The RBSP payload will provide essentially all of the required measurements, especially high-energy electrons and very high-energy protons from REPT through the flight of a payload with extensive energy resolution for both electrons and ions. Especially important are measurements from the under-sampled MEO region, which can provide a link to more extensive measurements at GEO (Geostationary Earth Orbit) and can hence lead to the development of more accurate specification models that are valid into the heart of the outer and inner radiation belts (industry requires MEO satellite lifetimes to be around 10 years).

2.2 REPT Measurement Requirements

The science background and data requirements described above impose significant demands upon the REPT instrument. The proposed sensor elements must fit naturally into the overall RBSP payload and thereby contribute to a complete suite of instruments on the spacecraft. The combination of the REPT instruments and the others on RBSP will address all of the key questions of electron acceleration, electron loss, and ring current effects in a broad space weather context.

Based on long-term observations of SAMPEX and geostationary orbit satellites, the averaged radiation belt intensity has a strong solar cycle variation (Baker et al. 1987, 2007; Li et al. 2001b). REPT must provide pitch angle and energy-resolved particle measurements

near the equatorial plane that can be projected to higher latitude, giving a complete 3-D spatial distribution. The measurements of RBSP will be used to validate existing specification models and calibrate with measurements from spacecraft at other orbits, such as GOES and POES, which have longer mission lives. REPT measurements will aid the global specification of the radiation belts especially at the relativistic and ultra-relativistic energies.

A fundamental goal of the RBSP mission is to differentiate among competing processes affecting the acceleration and transport of radiation belt electrons in the outer zone (Mauk et al. 2012). Crucial to this analysis is obtaining radial profiles of the phase space density of the radiation belts, properly ordering the observations in the three adiabatic invariants μ, K, and L (Roederer 1970). The quantities K and L depend on the global magnetic field configuration, and are particularly sensitive to variations in the model used in their evaluation (Green and Kivelson 2004). Further, these properly-ordered phase space density observations must be made with sufficiently high temporal cadence to capture the sometimes hours-long evolution of the belts and distinguish between features (peaks) in the phase space density profile that result from losses at high L, in contrast to those that result from internal acceleration mechanisms at lower L.

The goal for the REPT design therefore is to measure thoroughly the directional intensities and energy spectra of $\sim$1 to $>$10 MeV electrons throughout the slot and outer radiation belt region. To do this, the instrument requires an adequately large geometric factor to get reasonable count rates above background at the higher energies and yet must not saturate at the lower energy ranges. Thus, there must be a balance between foreground saturation on the one hand and background dominance on the other. There must be fast enough electronics to avert undue dead-time limitations and chance coincidence effects.

Some key features about the REPT design can be described by referring to Fig. 2. As noted previously, the REPT instrument must have an optimized geometric factor in order to

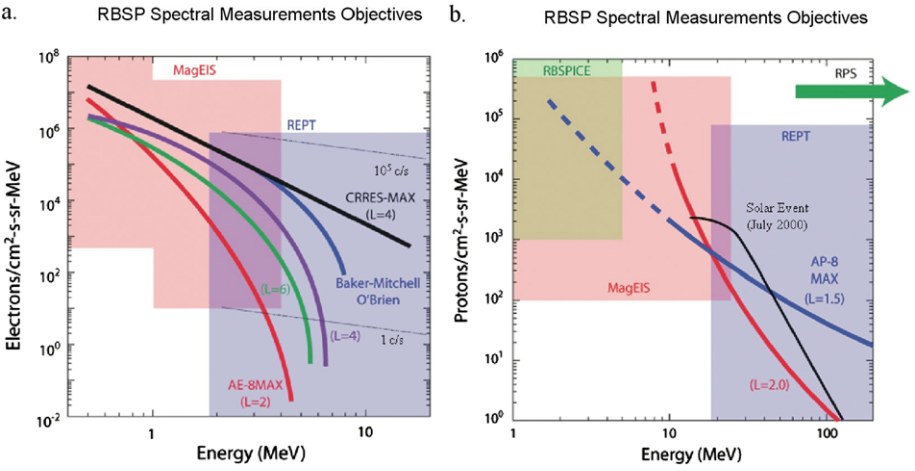

Fig. 2 (**a**) The kind of differential electron energy spectra that REPT will need to measure. The several different colored curves in the plot show model spectra (from AE-8 MAX) and also show two extreme spectra (CRRES-MAX and Baker, 2008), which were derived from the most intense events observed in such periods as the March 1991 case discussed previously. The *blue-shaded rectangle* in the figure shows the flux vs. energy domain that is expected to be measured by REPT in order to cover the requisite energy and intensity ranges (the actual measurement capabilities are described in detail in the instrument section). The *pink shaded rectangles* show for reference the flux-energy intervals that will be covered by the Magnetic Electron Ion Spectrometer (MagEIS) that will also be part of the RBSP payload (see Blake et al. 2012); (**b**) Similar to (**a**) but for protons

cover a wide dynamic range of electron fluxes that may be encountered. As shown in the figure, it is ideally the goal to cover a range from $\sim 10^{-2}$ to over 10^6 electrons/cm^2 s sr MeV. This will give REPT the sensitivity to handle expected fluxes (on the low end) in the radiation belt slot region and also out near spacecraft orbital apogee, while also being able to measure without compromise the most extreme possible spectra that might occasionally occur in the heart of the outer zone ($L \sim 4$) during events such as the March 1991 event.

Other key points to note are that REPT must be designed to avoid substantial deadtime effects in the sensor system. This means that for the highest flux cases (for $L = 3$–4) the electronic signal rates due to electrons in the energy range ~1–5 MeV must be nearly linear (within 10 % or so) in their responses up to at least 2×10^5 counts/second (c/s). It is also clear from Fig. 2 that electron fluxes in the 0.5 to ~1.5 MeV energy range (i.e., the energies just below the REPT energy threshold) could cause significant pileup effects (Vampola 1998) in the REPT sensors. This would probably be worst around the peak flux region at $L \sim 4$. Closely related concerns revolve around having such high single detector counting rates that chance coincidences (Vampola 1998) of counts in the individual detectors lead to false counts in the REPT energy channels. Such chance coincidences can result either from having high background singles rates due to side penetration through physical shielding or it can result from penetration of lower electrons into the detector telescope stack through the front entrance aperture. Finally, a very significant concern is the generation and counting of bremsstrahlung photons (in the X-ray range) generated by incident high-energy electrons. Such bremsstrahlung can itself cause very high and debilitating pulse pileup and side-penetration backgrounds in individual detectors. As will be discussed in detail below, we have carefully designed REPT so as to minimize all of these possible problems with a solid-state detector telescope.

We also have designed REPT to measure the very high-energy proton populations that will be encountered by the RBSP spacecraft. These high-energy protons will be seen primarily in the region known as the "inner" Van Allen radiation zone, which is essentially in the magnetic confinement region at $L \leq 2$. The other situation when very high-energy ($E \geq 20$ MeV) protons will be encountered is when intense solar energetic particle (SEP) events are in progress. Figure 2b illustrates differential directional proton intensities versus proton kinetic energies. Two typical proton spectra, one for $L = 2.0$ and one for $L = 1.5$, are shown by the colored curves based on the AP-8 MAX model (Vette 1991). Also shown by the black curve is the observed proton energy spectrum for an SEP event in July 2000 (Mewaldt 2006). The figure also shows with the blue-shaded rectangle the proton flux-energy domain that REPT will cover. The pink-shaded area shows the domain to be covered by the MagEIS ion sensors (Blake et al. 2012) while the green-shaded area shows the domain to be covered by the RBSPICE instrument on board RBSP (see Lanzerotti et al. 2012).

From Fig. 2b we see that by far the "hardest" proton spectrum expected to be encountered by RBSP will be the inner zone region around $L = 1.5$. In that area—near the perigee for the RBSP orbits—the spacecraft and sensor systems will be exposed to a spectrum of protons extending up to well above 100 MeV in energy. REPT has been designed to have the energy coverage (17–200 MeV) and dynamic range (10^0–10^5 protons/cm^2 s sr MeV) to measure most of the inner zone proton population. REPT will also be able to measure the SEP events likely to be encountered.

As for the electron design considerations discussed in relation to Fig. 2a, we note that similar concerns arise for proton sensor design. Thus, we have chosen a geometric factor which helps assure that neither inner zone proton spectra nor SEP events will ever lead to high enough counting rates to cause nonlinearity due to detector dead time. Also—even for

the worst-case energy spectrum at $L \sim 1.5$—we must assure that lower energy protons (below our designed energy threshold $E \sim 17$ MeV) will not pile up to cause false signals. As for the electron case, we also must design the side shielding and the front sensor aperture to assure that background and single detector rates will never lead to high chance coincidence rates in the proton detection channels. Our discussion of the detailed REPT design (below in Sect. 3) will show that we have carefully dealt with these challenging issues and should have clean proton measurements and acceptable background rates under almost all foreseeable circumstances.

2.3 Anticipated REPT Science Results

As noted above, a well-designed REPT instrument will provide precise and unambiguous measurements of energetic electron fluxes in the energy range ∼1.5 to ∼20 MeV. By providing accurate energy spectra as well as detailed pitch angle information, it will be possible at each spatial location of RBSP to specify the near-equatorial, directional electron intensity, j. Using concurrent magnetic field strength, B, measured by RBSP, the phase space density (f) can be specified for a given value of the first adiabatic invariant (μ, also known as the magnetic moment):

$$f = j/p^2 \tag{1}$$

where p is the relativistic momentum. This becomes approximately

$$f(\mu) = \frac{j}{\mu B}. \tag{2}$$

This phase space density at constant first invariant (constant μ) is perhaps the single most important derived quantity from the RBSP payload for radiation belt studies (e.g., Roederer 1970). Examining $f(\mu, t)$ allows tremendous insight into radiation belt dynamics, sources and sinks of particles, and mechanisms of acceleration and transport.

Figure 3 is an example of the range of phase space densities that might be encountered for electrons that fall in the REPT kinetic energy range (∼1.5–20 MeV). The red colored

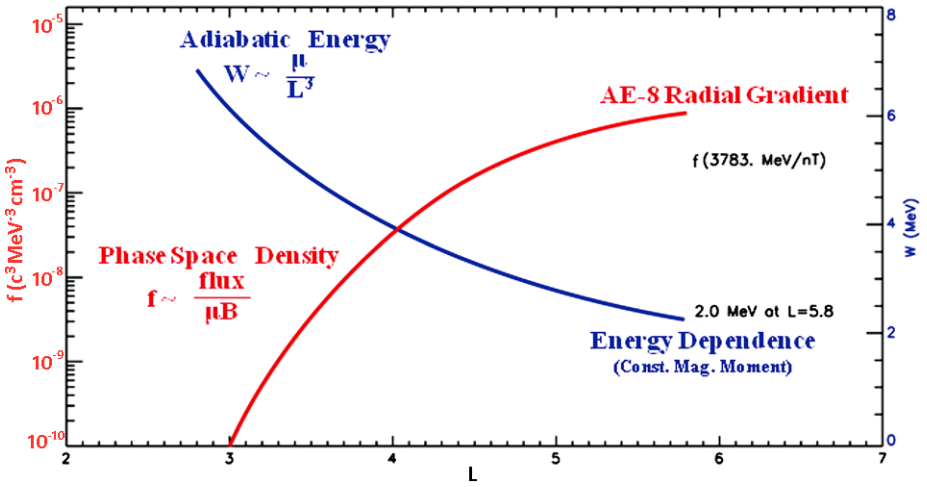

Fig. 3 Phase space density (*red*) and adiabatic energy (*blue*) variations expected over the L-value range to be explored by the RBSP spacecraft (see text)

profile in Fig. 3 shows what a widely adopted radiation belt model (AE-8) would say is the profile of phase space density as a spacecraft such as RBSP went from apogee ($r = 5.8R_E$) near the equator inward to $L \sim 3$. As can be seen, for the particular value of magnetic moment chosen ($\mu = 3783$ MeV/nT), the radial gradient would be such that $f(\mu)$ would go from $f \sim 10^{-6}c^3$ MeV^{-3} cm^{-3} at $L = 5.8$ to $f \sim 10^{-10}c^3$ MeV^{-3} cm^{-3} at $L = 3.0$, where $c = 3 \times 10^8$ m/s (the speed of light).

We also note the corresponding blue curve in Fig. 3. This shows the kinetic energy that an electron moving "adiabatically" along an equatorial pathway from $L = 5.8$ to $L \sim 2.7$ would have. In this case, an electron having $\mu = 3783$ MeV/nT would have a kinetic energy (which we designate here by W) of $W \sim 2.0$ MeV (see vertical axis to the right in Fig. 3) at $L = 5.8$. The electron undergoing adiabatic transport from $L = 5.8$ to $L \sim 3.0$ would gain energy (due to conservation of the first invariant), going as $W \sim \mu/L^3$. At $L = 2.7$, the electron would have an energy $W \sim 7.0$ MeV. Transporting such an electron even more deeply into the magnetosphere, down to $L \sim 2.0$ would bring an electron of this magnetic moment to the upper energy range covered by REPT, i.e., above ~20 MeV.

This figure makes the crucial point that to study consistently and thoroughly the transport, acceleration, and loss of electrons of even relatively modest energies (0.5–2.0 MeV) near geostationary orbit ($r = 6.6R_E$), we must be prepared to follow such electrons up to quite high energies (15–20 MeV) deeper in the magnetosphere. It is most effective and unambiguous to follow such electron transport by using a single detector system that self-consistently measures the electron population transport all the way from RBSP apogee to near RBSP perigee. REPT is designed in this spirit.

A key remaining question that the REPT team has addressed is: "How precisely must we be able to determine phase space densities at various points along the RBSP trajectory?" Figure 4 shows one answer to this question. Underlying the green and blue shaded curves in Fig. 4 is a red profile. This is the same "radial gradient" curve based upon the AE-8 model that was shown in Fig. 3. Using the expected effect of strong radial diffusion (as might result

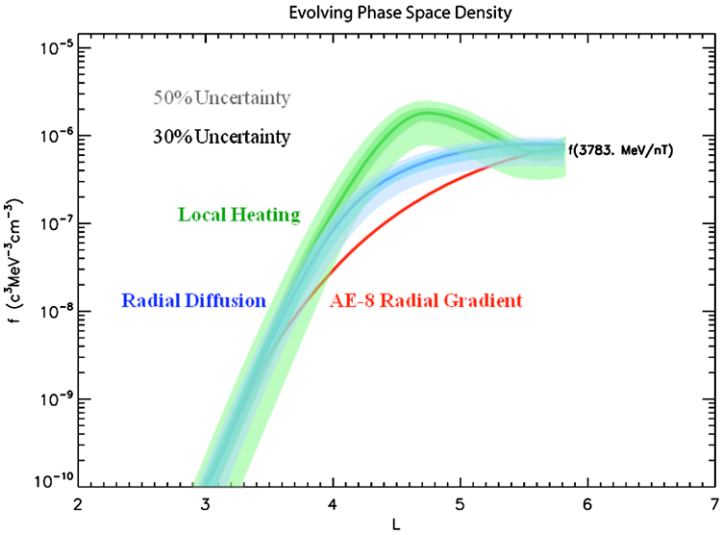

Fig. 4 A figure showing expected equilibrium (*red*) phase space density profile plus the enhanced profiles that might result from enhanced radial diffusion (*blue*) or intense local wave heating (*green*). The effects of REPT measurement uncertainties are shown by the *blue* and *green shading* as described in the text

from ULF wave transport) we show in blue, in Fig. 4, the change that might occur for an enhancement derived from the red curve. Similarly, if we model how VLF waves might locally heat the expected equilibrium (red) electron phase space profile, the green curve shows the "local heating" model curve.

The shaded bands around the main radial diffusion (blue) and local heating (green) curves attempt to show what 30 % and 50 % uncertainties in the REPT electron measurements would imply about derived phase space densities. From such modeling and analysis, we conclude that REPT flux measurement must be made with absolute accuracies in the 20–30 % range. Larger uncertainties in REPT fluxes (i.e., extending up to 50 % uncertainties or greater) would completely prohibit us from distinguishing between radial diffusion and local heating mechanisms. As will be seen below, the REPT science and engineering teams have succeeded in devising REPT flight units for the two RBSP spacecraft that are built and calibrated to a precision ($\leq$20 %) such that the scientific requirements of the mission are more than met.

2.4 Modeling

The RBSP mission will provide an unprecedented view of the dynamics of the radiation belts and the fields and waves associated with those changes. Detailed models of wave/particle interactions (e.g. Horne and Thorne 1998; Bortnik et al. 2009; McCollough et al. 2010; Elkington et al. 1999) and transport processes (Elkington et al. 2005; Li et al. 1998; Sarris et al. 2002) can provide insight into which physical processes are likely to be important in the energization and loss of the particles comprising the radiation belts. However, direct RBSP observation of the important phenomena will still be limited to processes taking place at the satellite locations. As particles drift about the Earth they will encounter and be affected by fields and waves that may be principally occurring in regions away from the spacecraft observation locale at a given moment of time, but still affect the particles that drift across the spacecraft location. Further, many transport processes require knowledge of the large-scale configuration of the waves and fields guiding the radiation belt particle motion, such as is the case with ULF wave mode structure in determining rates of radial diffusion (Elkington et al. 2003). Dynamic models of the global state of the magnetosphere will therefore be necessary to provide context for interpreting changes observed at discrete locations of the RBSP spacecraft.

At present, the most capable physically-based magnetospheric simulation codes are based on the MHD approximation. Global MHD models provide a dynamic, physically-based means of estimating the global configuration of the magnetosphere (e.g. Lyon et al. 2004; Gombosi et al. 2002; Raeder 2003). MHD simulations treat the fields and plasmas surrounding the Earth as a magnetized fluid (Sturrock 1994), allowing a computationally-tractable means of simulating the Earth's magnetosphere as it responds to changes in the solar wind. The MHD approximation does not allow full specification of all the microphysical processes that may affect the radiation belts (e.g. those processes occurring at spatial scales below the ion gyroradius), but does include many important effects known to influence the radiation belts and its boundary populations, including magnetic reconnection, global magnetospheric convection, and the solar wind driving of large-scale waves that can lead to the transport and energization of radiation belt particles. These simulations can be driven by solar wind observations upstream of the bow shock, providing a realistic link between solar wind driving of the magnetosphere the time evolution of the simulated fields.

In Fig. 5 we show how a global MHD simulation may be used to study the effect of differing boundary populations on radiation belt evolution during a hypothetical storm driven

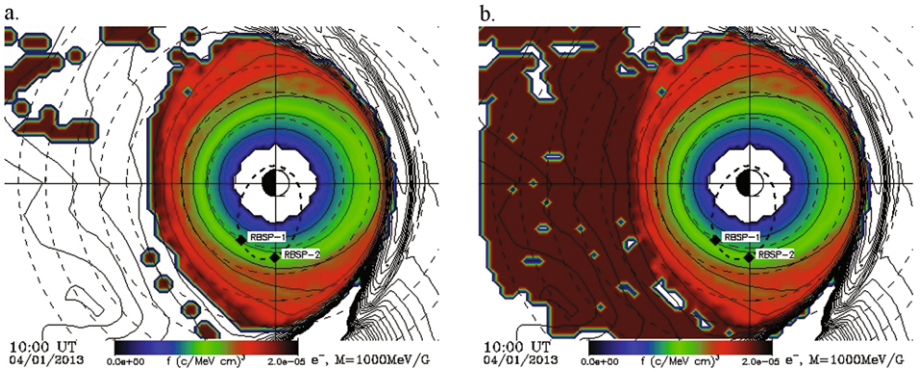

Fig. 5 Global MHD/Particle simulations showing the evolving phase space density in the equatorial plane for energetic electrons of 1000 MeV/G for a hypothetical RBSP orbit configuration. (**a**) Shows conditions where the trapped radiation belt particles are subject to an open boundary condition, allowing particles to be lost from the inner magnetosphere via outward radial diffusion. (**b**) Indicates the effect of plasma sheet particles convectively injected into the inner magnetosphere, augmenting the radiation belt populations in the trapping region

by a high-speed solar wind stream interacting with the magnetosphere. Here we use the LFM MHD simulation (Lyon et al. 2004) coupled with test particle simulations to study the dynamic evolution of the radiation belts in a manner similar to that described by Elkington et al. (2004). In the left hand panel of Fig. 5a we show a snapshot of the simulated state of the radiation belts with an open boundary condition, where trapped energetic electrons are subject to only outward radial diffusion at the trapping boundary, which results in a net loss of particles from the radiation belts (Shprits et al. 2006). In the right-hand panel of Fig. 5b we illustrate a contrasting magnetospheric state where energetic particles from the plasmasheet are convectively transported Earthward, and form a positive boundary population for the radiation belts in the near-Earth tail. In both these figures, the magnetosphere is viewed from the pole, with the phase space density of particles of a given first adiabatic invariant (1000 MeV/G) displayed on the color scale and contours of constant magnetic field strength indicated by solid lines. The locations of the two RBSP spacecraft in this interval are indicated by labeled black diamonds, along with the orbit trajectory (bold dashed line) and contours of constant radial distance (light dashed lines forming concentric circles about the Earth). The trapped population in these figures was modeled as a monotonically-increasing distribution function, with a plasmasheet population exceeding the phase space density at geosynchronous consistent with the observations reported by Taylor et al. (2004). The inner boundary of this simulation is at approximately 2.3 Earth radii from the center of the Earth.

In Fig. 6 we show the simulated magnetic fields (dotted lines) and electron phase space densities (solid lines) observed over several orbits at one of the virtual RBSP spacecraft locations. Over the course of a single orbit the phase space density can be seen to generally rise, and the magnetic field decrease, as the spacecraft moves radially outward, reversing this trend on the inward legs of each orbit and reflecting the outward gradient in the assumed initial radiation belt electron population. Figure 6a indicates that the peak phase space densities decrease over the several orbits comprising this simulation, and suggests the effect of outward radial diffusion on radiation belt losses under these driving conditions. By contrast, Fig. 6b shows peak phase space densities increasing with time, illustrating the

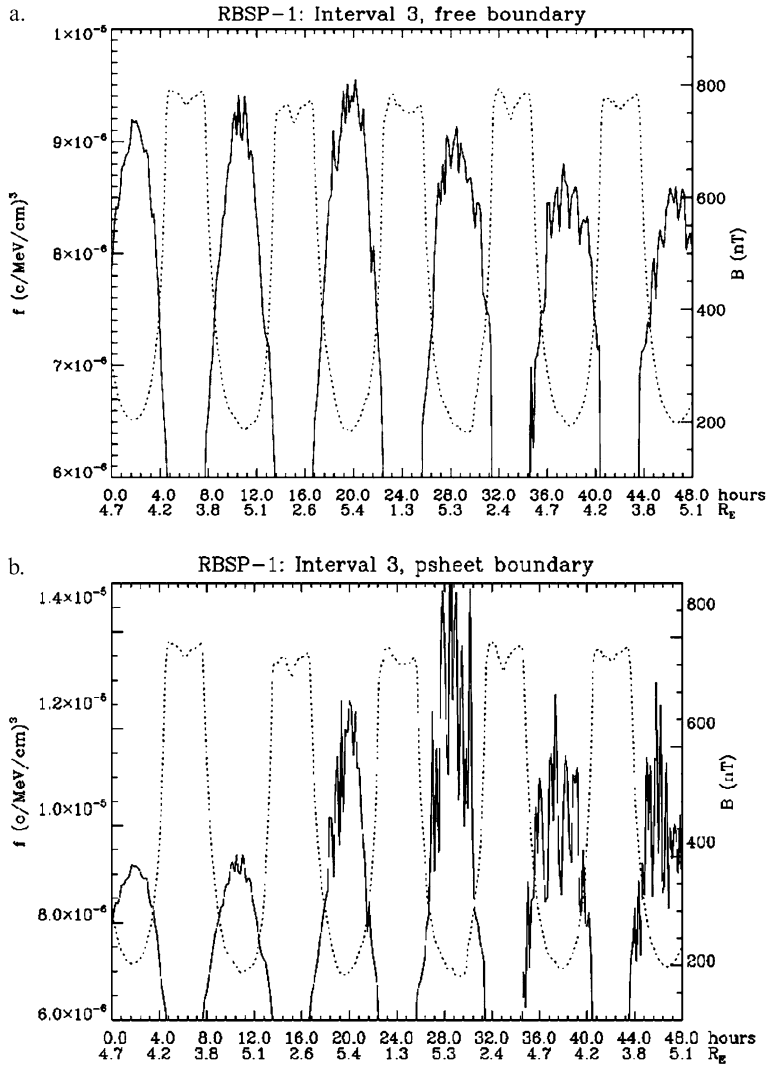

Fig. 6 Virtual phase space densities and magnetic fields observed by the modeled RBSP spacecraft indicated in Fig. 5. (**a**) Shows decreasing phase space densities over several orbits, resulting from particles lost to outward radial diffusion at the open trapping boundary. Increasing phase space densities in the right hand panel (**b**) suggest what might be seen under conditions of plasma sheet access to the inner magnetosphere

effect of plasma sheet particles being trapped in the inner magnetosphere and the resulting contribution to pre-existing radiation belt populations.

At present, the global simulations illustrated here do not include all physical processes currently thought to be important in the dynamics of the radiation belts (e.g. heating via chorus emissions or losses due to EMIC waves); however, they do provide a means of quantifying changes in the distribution function that might occur under the conditions of pure outward radial diffusion and loss through the trapping boundary, or the convective injection of particles from the plasma sheet. The differences between the results of these simulations

and actual observations from the REPT instrument can be used either to infer other physical heating and loss processes that may be occurring in local times and locations beyond the view of the RBSP spacecraft, or to infer that such processes are not required to explain the variations observed during particular events or intervals.

3 Instrument Description

3.1 Instrument Design and Modeling

Obtaining precise spectra and angular distributions is critical for determining the electron and proton phase space densities necessary to answer the important science questions posed above. This is particularly difficult in the inner magnetosphere where the radiation is very penetrating and intense. The high fidelity measurement requirements combined with the hostile environment of the inner magnetosphere has led us to choose passivated ion implanted silicon particle detectors in a particle telescope con-figuration to measure electrons and protons in the energy ranges ∼1–20 MeV and ∼17–200 MeV respectively (the exact energy ranges of all the electron and proton differential channels are listed in Table 7). We employ pulse height analysis techniques to separate electrons from protons and use carefully designed shielding to limit particle background expected in this high radiation environment.

A compact solid-state telescope system is ideal for measuring very high-energy particles, since other approaches such as particle magnetic spectrometers would require high magnetic fields, which result in massive instruments. The REPT therefore consists of a stack of silicon solid-state detectors in a telescope configuration, a collimator, and a thick case surrounding the detector stack to shield the sensor from penetrating radiation and bremsstrahlung. The dimensions of the collimator determine the geometry factor. As mentioned previously (see Sect. 2), REPT measurement requirements constrain the geometry factor. We have optimized the geometry factor based upon electron measurements both at high altitudes and by extrapolating low-altitude observations (Kanekal et al. 1999). The instrument points perpendicular to the spin axis of the spacecraft and will sample all pitch angles of particles during almost all expected magnetic field orientations. The REPT will be used in a closely coordinated way with the MagEIS sensor that is part of the RBSP payload (Blake et al. 2012).

Figure 7 shows the REPT detector system concept in cross-section. The design is based on extensive experience of our team with prior space missions such as CRRES, POLAR, and SAMPEX. The Proton-Electron Telescope (PET) onboard SAMPEX (Cook et al. 1993)

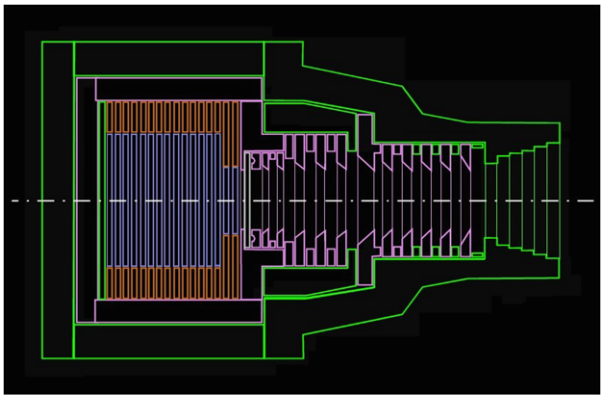

Fig. 7 REPT geometry in cross section implemented in GEANT4. Material marked in *green* is aluminum, *purple* is Hi-Z, *white* is beryllium, *brown* is polyimide and *blue* is the silicon detectors

operated very well for over 17 years from the time of spacecraft launch in 1992. It provided close heritage for the REPT. Lessons learned from the PET/SAMPEX experience (Baker et al. 1993, 1994) helped guide our design on the REPT for the more intense and higher background environment that will be experienced by RBSP near the magnetic equator compared to the low-altitude (∼600 km) SAMPEX orbit. Furthermore, detailed simulation of the instrument response to energetic particles was made using GEANT4 (GEometry ANd Tracking) (Agostinelli et al. 2003) to not only design the basic configuration but also to establish instrument characteristics.

Figure 7 shows the REPT instrument geometry that resulted from optimizations using GEANT4 simulations. The REPT collimator was designed to yield a geometry factor of 0.2 cm^2 sr with a resulting circular conical FOV of 32°. At the back of the collimator is a carefully chosen aperture-covering beryllium (Be) window that excludes lower energy electrons ($\lesssim$1 MeV) and protons ($\lesssim$15 MeV). The silicon detectors (labeled R1 through R9 numbered from the front) are stacked behind the Be window, the first being 1.5 mm thick and 20 mm in diameter with annular concentric designs. The front detector, which is 7 cm from the front of the collimator, determines the geometry factor. The design is analogous to the PET, although the REPT has a narrower field of view (32° for REPT compared to 58° for PET). The geometric factor for REPT is about five times smaller for 1–5 MeV electrons than it was for PET.

It is well known and understood that electrons scatter considerably as they interact within detector systems and deviate considerably from their original direction. Thus, electrons may "leak" out of the detector stack. We have designed the REPT with larger-area detectors R3 to R9, which are 40 mm in diameter and are twice as thick as the front detectors. This results in higher detection efficiency for the 5–20 MeV electrons that are a key target of the RBSP and LWS programs. These larger detectors actually comprise a pair of 1.5 mm thick detectors whose signals are electronically summed.

The REPT detector stack is therefore comprised of 24 mm of Si, which will stop most electrons of energy up to 10 MeV. However, as determined by our GEANT4 simulations, by imposing selection criteria on energy deposition in the detectors comprising the stack, the REPT can detect electrons in differential energy bins up to 20 MeV and protons up to 115 MeV. Higher energy electrons and protons above these values are measured as integral channels. Our goal has been to focus design attention on 1 to 20 MeV electrons. We have set differential energy channels with $\Delta E/E = 0.3$ giving 11 electron energy channels in the target energy range. The designed geometric factor of $g \sim 0.2$ cm^2 sr gives a dynamic range at $E \sim 2$ MeV of ∼100 counts/s for "weak" enhancements near $L = 4.0$ and $>10^5$ counts/s for some of the strongest events we have detected in recent times (cf., Baker et al. 2004 and Fig. 2 above).

An important design consideration is to suppress backgrounds due to directly penetrating radiation and bremsstrahlung. The REPT has been built with gradated side shielding to greatly reduce electrons below ∼20 MeV (and protons below ∼140 MeV). The inner layer of shielding is a high-Z metal (tungsten-copper alloy) to stop bremsstrahlung X-rays, while the outer shielding is aluminum to provide good stopping power while reducing initial bremsstrahlung production. The shielding thickness has been optimized using GEANT4 with a realistic REPT geometry to obtain detection efficiencies for side-penetrating electrons and protons. Singles rates due to side penetrating electrons are about 1 to 2 orders of magnitude lower than the FOV electrons for assumed extreme spectrum (Baker et al. 2008) for the front detectors ($\sim 10^3$ s^{-1}) and are comparable in magnitude for detector R4. Coincidence requirements on the front detectors ensure that the REPT differential energy channels have negligible background even in this extreme scenario. The minimum energy required

to penetrate the shielding varies from ∼100 to ∼150 MeV for protons incident at 0° up to 75° from perpendicular. We have also calculated the expected background from high-energy galactic cosmic ray protons using measured proton spectra (Alcaraz et al. 2000) and found them to negligibly small with singles rates ranging from 20 to 50 s^{-1}, compared to $\sim 10^3$ s^{-1} for the nominal AE8 (Min) FOV electrons at $L = 4$. Our goal has been to maintain high foreground/background ratios even during the most intense radiation belt enhancement events and for passages through the powerful inner zone.

3.2 Sensor Synergy and Proton Detection

The REPT measurement of electrons will have important energy overlap with the MagEIS detector system (Blake et al. 2012). This will afford key redundancy in the crucially important 1.0–4.0 MeV electron energy range. It will also allow good on-orbit cross-calibration between these two highly complementary sensor systems. The REPT will provide the essential measurements of the high-energy portion of the radiation belt electron population with higher sensitivity (larger geometric factor) than MagEIS.

The REPT also has overlapping measurements of protons with the RPS sensor (Mazur et al. 2012, this issue) in the 50–120 MeV range, which is covered by 3 differential channels of REPT. In addition REPT provides integral measurements of protons above ∼115 MeV.

3.3 Design Overview

A cut-away of the REPT instrument layout is shown in Fig. 8. The collimator, beryllium window, detectors and sensor shielding, as previously discussed, are toward the top of the

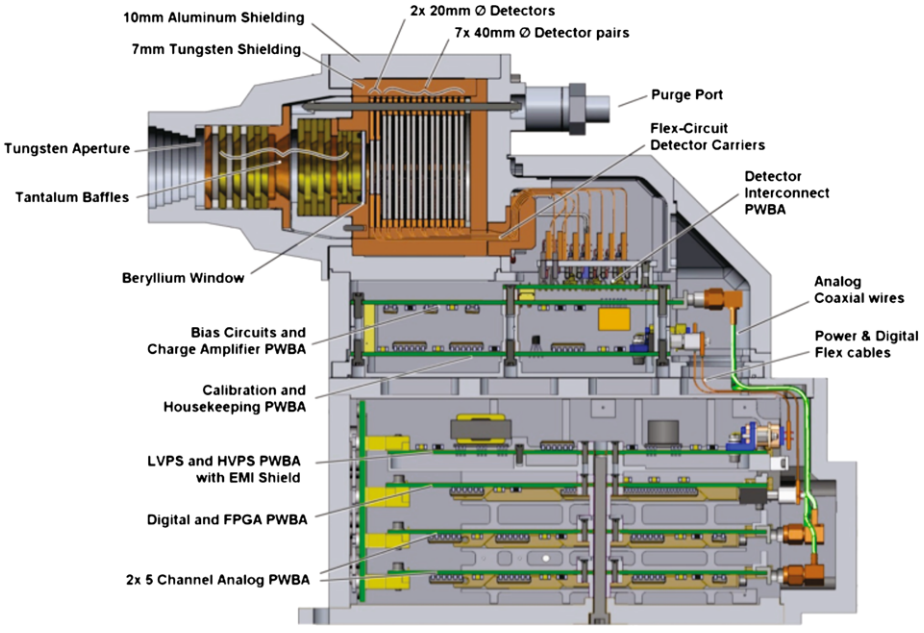

Fig. 8 Cut-away of REPT showing high-Z disk-loaded collimator, detectors and shielding along with the supporting electronics. Charge sensitive amplifiers, bias, and calibration circuitry is located near to the detectors. The balance of the analog circuitry along with the low voltage power supply and FPGA are housed in the lower electronics box

figure. The output signal from each of the detector planes is collected by individual charge sensitive amplifiers (CSA) and the output of each CSA drives parallel fast- and slow-pulse shaping circuits. The fast circuits provide event detection for each detector while the slow circuits provide noise filtering and pulse height analysis (PHA). The fast signals are routed to a field-programmable gate array (FPGA) which implements detector-to-detector coincidence detection monitors for pile-up events to determine the occurrence of valid events, and coordinates the analog to digital conversion (ADC) sampling of each of the slow (PHA) channels.

A valid event occurs when one or more detectors exceed threshold within a coincidence window (see section on Timing, Coincidence and Pile-up). For valid events the FPGA compares the set of PHA values against twenty configurable logic statements, (see Tables 2 and 3) each designed to qualify a particle into a particular species and energy range. Each spin of the spacecraft is divided into 36 sectors. The tally of positive logic statement evaluations is collected over a spin sector and the 36 sector results are reported in primary science telemetry. Along with the energy bin count rates, the primary science includes the individual detector event rate, i.e., singles counts, by sector. A secondary science product, a sampling of PHA data sets with the associated energy bin results, is collected on a nominal 2 sets per second cadence.

All REPT functionality is implemented in an FPGA thereby eliminating the need for a microprocessor and software. Separate state machines support science data processing, housekeeping data collection, data packetization and telemeterization, commanded memory reading and writing, and spacecraft spin synchronization. With only two modes of operation, Safe and Run, REPT operations and commanding is kept to a minimum.

Figure 9 shows the REPT flight model A (FM-A) just prior to integration to the RBSP-A spacecraft. Each REPT instrument is situated on its spacecraft anti-sun deck with electronics box inside the spacecraft and the sensor and collimator passing through the deck. The instrument is aligned to be parallel to the deck and perpendicular to the spacecraft spin axis (see Fig. 10).

The REPT specifications, properties, and requirements are given in Table 1. The energy resolutions for electrons and protons are better than required for science measurements. With the FOV and geometry factor dictated by low-end electron fluxes, meeting the counting rates associated with high fluxes, with acceptable dead time losses, was a driving design factor. The allocated data rates for REPT easily support low volume of fixed rate housekeeping data, and primary science data rate that varies with spacecraft spin rate. A secondary-science PHA data packet is included in the telemetry plan whose length will be adjusted to keep the total rate within allocation. The instrument power requirements are well under the allocated limits and, with generous mission mass allowances to accommodate mandated electron deep dielectric shielding, REPT is heavy but well under its mass limits.

3.4 Sensor Design

The sensor head, the portion of the instrument positioned on the exterior of the spacecraft, includes the detectors, their shielding and the collimator, the beryllium window to block low energy electrons, a dry nitrogen purge port and plenum to keep the detectors dry, and three circuit boards: the Detector Interconnect PWBA, (Printed Wiring Board Assembly) the Bias and CSA PWBA and the Calibration and Housekeeping PWBA.

3.5 Detectors

The detectors, shown in Fig. 11, are ion-implanted high-resistivity 1500 µm thick silicon diodes manufactured by Micron Semiconductor LLC, U.K. Made with Micron's 2M pro-

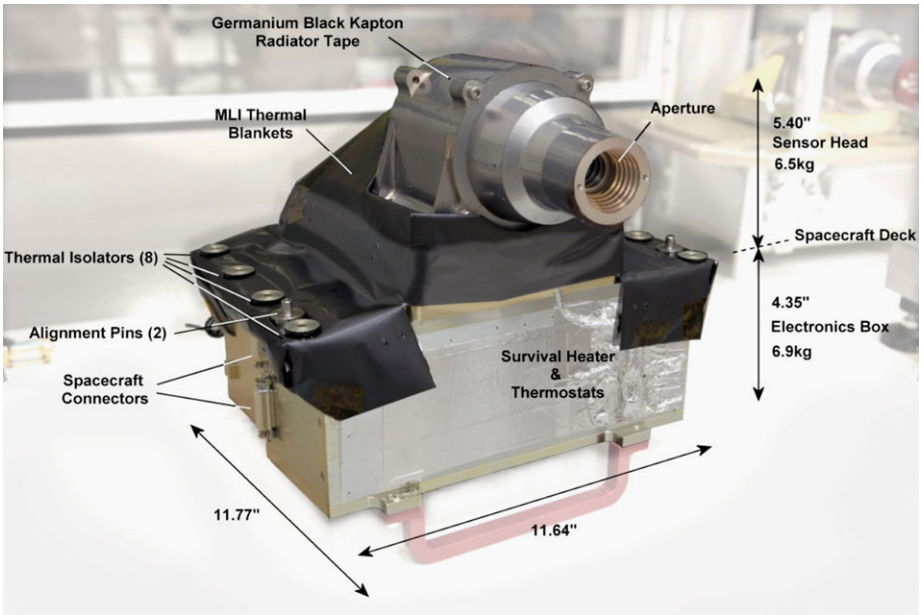

Fig. 9 REPT flight unit 'FM-A'. The upper section, in grey, is the sensor housing with the collimator aperture facing forward. The lower portion is the electronics box sitting on red tag handles that are removed after instrument installation to the spacecraft. The black flight multi-layer insulating (MLI) thermal blankets are seen draped over the box. Spacecraft communication and power cables attach at the left and on the right hand edge of the box front survival heater power and spacecraft monitored temperature sensors attach

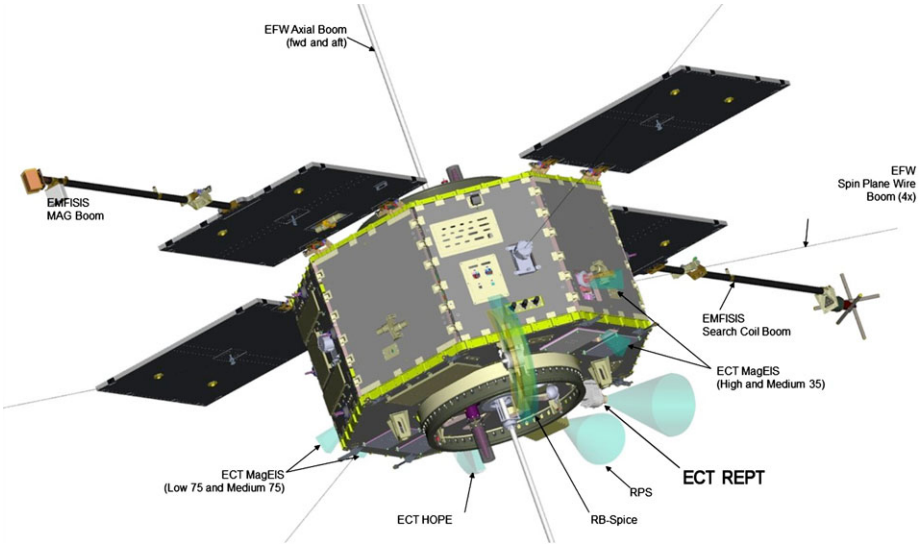

Fig. 10 RBSP Spacecraft showing location of REPT instrument

Table 1 REPT summary specifications

Parameter	Delivered	Level-1 requirements
Proton energy range	17 MeV to >100 MeV	≤40 MeV up to ≥75 MeV
Proton energy resolution ($\Delta E/E$)	30 %	$\Delta E/E < 30$ %
Electron energy range	1.6 MeV to >18.9 MeV	≤4 MeV up to ≥10 MeV
Electron energy resolution ($\Delta E/E$)	25 %	$\Delta E/E < 30$ %
Geometry factor	0.2 cm^2 sr	
Field of view	32° (Full angle)	
Integration cadence	1/3 s nominal (1/36 of spacecraft spin period)	≤1.0 min but an integral number of spins
Spin plane angular resolution	36 sectors	≥8 sectors per spin
Dead time losses	∼20 % at 100 kilocounts s^{-1}, correctable to <5 % 50 % at 350 kilocounts s^{-1}, correctable to <20 %	<30 % including errors at AE8max, $L = 4$, 4 MeV
Mass	13.4 kg	
Power	6.2 W, not including survival heater	
Data volume allocation	1580 bps maximum	
Dimensions	$11.77'' \times 11.64'' \times 9.75''$	

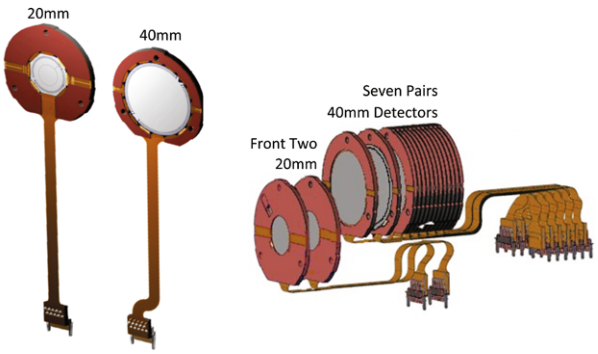

Fig. 11 REPT solid-state detectors in rigid-flex packages. Detector cathode faces are shown in figures at *left*. *Figure on right* shows detector stacking and flex routing out of the shielding

cess, the implantation dead layer is less than 0.5 µm and the full surface sputtered aluminum metallization is nominally 0.3 µm thick. The design includes their proprietary MGR guard ring design that reduces noise from edge leakage paths. The flight detectors came from a number of different silicon boules with different resistivity so depletion voltages varied from 120 V to 300 V. Room temperature leakage currents at full depletion are <0.5 µA on the 40 mm detectors and <0.1 µA on the 20 mm models. Studies show that by the end of RBSP mission life leakage current on the most-irradiated front detector will increase by less than a factor of 10.

The detector packages are multilayer rigid-flex circuits custom designed for the REPT instruments. The rigid detector carrier portion of the package is 2.5 mm thick and precision machined to accurately register the detector silicon and for alignment within the REPT shielding. Electrical contact from the front and back of the silicon to the package is accom-

plished with low-profile triple-redundant bond wires. The approximately 5″ long two-layer flex portion of the package carries the electrical signals through the sensor shielding and to the Detector Interconnect PWBA.

The front two detectors in the sensor stack are 20 mm diameter silicon, custom designed for the REPT instrument. The active area is divided into two concentric regions of equal area with separate electrical connections off-chip to the package. For the second detector in the stack the two active areas are tied together on the Detector Interconnect PWBA but the two active areas on the front-most detector have fully independent electronics channels. The smaller active areas allow much improved pile-up detection at high fluxes. For valid events the PHA values are summed back together in the FPGA, accounting for any charge-sharing of a particle impacting near the boundary of the two active areas. The isolation gaps between the two active areas are ∼100 μm wide and cover less 1 % of the total detector area in order to minimize both the number of particles interacting with them and any charge collection losses. Our studies using electron and proton accelerator beam data, showed that less than 2 % of particle events showed any charge division between the two areas and the reconstructed energy of this group was indistinguishable from the larger population.

The 40 mm diameter detectors are standard devices from Micron Semiconductor mounted in the custom REPT rigid-flex package. Fourteen 40 mm detectors are used as pairs to make up the back 7 detectors. Each pair is electrically connected together in parallel and mounted in the detector stack cathode-to-cathode. This doubles the effective thickness while maintaining the charge collection time of the single thickness. The cathode-to-cathode mounting minimizes differential voltages between adjacent surfaces while also reducing crosstalk between adjacent pairs. Alternating the directions that the detectors face spreads the connectors away from each other for connection in the limited space of the Detector Interconnect PWBA.

All the flight candidate detectors were characterized for depletion voltage, leakage current, alpha particle response, noise and dead layer thickness and uniformity. Flight detectors were selected for in-family leakage current behavior over temperature and for depletion voltages. The 40 mm detector pairs were matched for depletion voltage and the individual bias circuits were adjusted for each pair to provide 30 V to 70 V over depletion from the common bias power supply. Bias voltage was limited to 70 V over depletion as beyond this leakage current became notably more temperature sensitive.

Modeling of charge transport and charge collection times, in the manner of Leroy et al. (1999), compares favorably with collection times measured for REPT detectors with 30 V over-depletion, giving values from 210–380 ns, depending on charge amplitude, temperature and which detector face the particle enters. Our measurements show (Fig. 12) that the time from the inflection point on the CSA waveform to full charge collection is consistently 170 ± 20 ns independent of particle type, incident detector face and temperature.

While the preceding discussion was based on measurements of electrons and alpha particles it was assumed the results would hold for protons. This was confirmed through proton accelerator testing (see Sect. 4), with a notable exception. During early proton beam tests it was observed that, at certain energies, charge collection did not behave uniformly throughout the detector stack. It was determined that high-energy protons penetrating into the stack but stopping after barely penetrating (20–50 μm) in the first of a pair of doubled detectors exhibited notably delayed charge collection. With the detector pairs mounted cathode-to-cathode, the leading face of a pair is the low-electric field n-type region. It was overlooked that ions stopping in this region can exhibit slow charge collection due to the high ionization density (Bragg maximum) shielding most of the charge from the accelerating fields. Charge collection is retarded by the rate of plasma erosion (Ammerlaan et al. 1963). The consequence

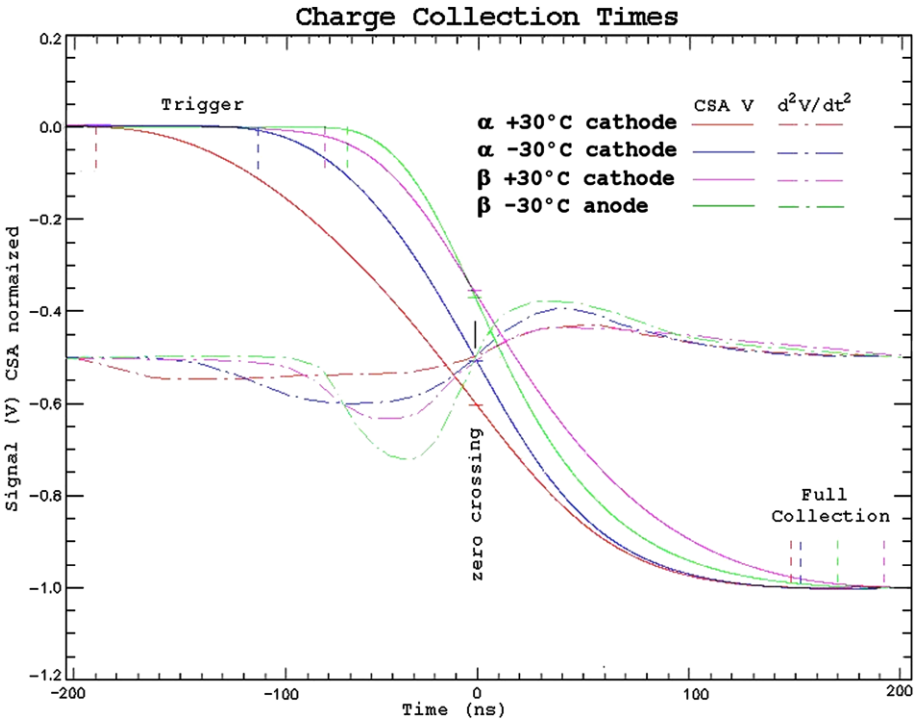

Fig. 12 Charge collection times measured in fully depleted 1500 micron thick solid-state detectors. Collection times from the inflection point of the charge current curve to full collection are roughly constant over particle type, temperature, and detector face

of this was that for a small set of very narrow proton energies REPT was mis-sampling the entire stack based on one delayed channel.

Event timing in the FPGA has since been modified to prevent this mis-sampling of the stack and, as described later, a scheme has been implemented to time any delay and correct the mis-sampling of any detector suffering slow charge collection.

3.6 Collimator

The sensor collimator is a high-Z disk-loaded design developed using GEANT4 modeling to verify scattering and cut-off energies and adjunct ray tracing to establish required material thicknesses for all paths. Disk spacing, edge bevel and aspect ratio were optimized to minimize lower energy range electron scattering (Vampola 1998) while material selection and thickness was chosen to provide a hard aperture for higher energy particles. Most of the collimator rings are made of tantalum. However tantalum is mechanically soft resulting in poor machining tolerance. Where precision is required, as with the front aperture-defining collimator ring, or where the part is structural like the mid-stack clamp, sintered tungsten alloys were used instead (see the following shielding section for a discussion of alloy selection). Toward the front of the collimator the spacers between the high-Z rings are aluminum to prevent scattering back into the collimator, but further down the collimator they change to tantalum to provide the necessary off-axis shielding.

At the back of the collimator, just in front of the detectors, sits the beryllium disk used to stop low energy electrons from overwhelming the front detector. The beryllium window is held in place by a Viton O-ring to provide a light-tight seal to the detector cavity.

3.7 Sensor Shielding

The REPT sensor shielding is made up of the 10 mm aluminum external housing and an inner 7 mm thick layer of sintered tungsten-copper (90 %–10 %) alloy. As pure bulk tungsten is very difficult to machine, the preferred form is one of several sintered alloys with a copper or a nickel/iron mix being the most readily available. A material activation study, undertaken at Brookhaven National Laboratory, showed that the unshielded W/Cu alloys may become activated (when exposed to radiation) but not when behind the 10 mm aluminum outer shielding. For the few tungsten parts in the collimator that do not have full aluminum shielding, we worked with the mission magnetics cleanliness team to fabricate these using a W/Ni/Fe alloy.

The back shielding plate is 9 mm thick to provide extra stopping power for the large surface of the back detector. Pressed into it are three tantalum rods with threaded ends, onto which the detectors are stacked, and which are used to hold the detector stack and shielding together. The detector flex circuits exit the shielding via a two-piece high-Z labyrinth affixed to the back plate. All shielding joints are stepped to eliminate any energetic particle sneak paths.

3.8 Bias, CSA and Calibration Electronics

The Detector Interconnect, Bias & CSA and the Calibration & Housekeeping (Cal & Hskp) PWBAs are mounted in the sensor head near to the detectors. Bias voltages from and detector signals to the Bias & CSA PWBA are routed through the Detector Interconnect PWBA. Electrical power, the common bias voltage and control signals for the sensor head are supplied to the Cal & Hskp PWBA via flex circuits from the Power and Digital PWBAs in the electronics box. The CSA outputs from all ten channels are routed to the two Analog PWBAs in the electronics box over individual 5″–6″ coaxial cables.

The 10 charge sensitive amplifiers on the Bias & CSA PWBA are the AMPTEK A250F that was selected for its speed, low-power characteristics and compact packaging. The CSA gains were adjusted to 36 mV/MeV (Si) with recovery time constants of ∼12 μs. Simulations show that with these values the CSA response remains linear for a 25 MeV (Si) event (expected maximum for a stopping proton) during a sustained 100 kcps 1 MeV (Si) flux. Side penetrating cosmic rays may deposit enough energy to drive the AMPTEKs out of their linear response range but testing shows they recover normally without signs of saturation delay for energies well above 100 MeV (Si).

A charge-injection circuit is part of the Calibration & Housekeeping PWBA for in-flight calibration tracking. The charge level is selectable from 0 to 25 MeV (Si) in increments of ∼83 keV. Upon command, 100 charge pulses are injected at the inputs of one or another set of 5 CSAs. The two sets of calibration channels are physically interleaved on the PWBAs supporting the monitoring of cross-talk. The FPGA collects events immediately following each of the 100 pulses and telemeters them to the ground as calibration data.

3.9 Electronics Box

The REPT electronics box contains the Power Supply PWBA, the Digital PWBA and two identical 5 channel Analog PWBAs and a backplane they all plug into. To mitigate deep

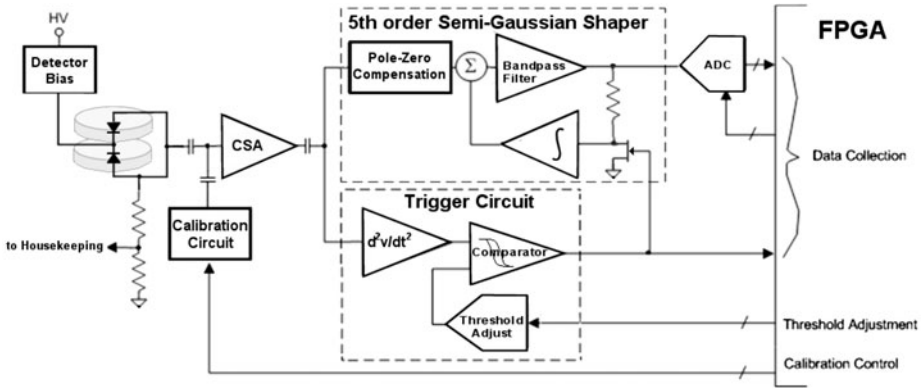

Fig. 13 One of ten REPT analog signal chains. Bias, CSA, and calibration circuitry is located in the sensor head. The shaper and trigger circuits, along with the ADCs are housed in the electronics box

dielectric charging of the PWBAs in the high electron flux environments, the walls of the electronics box, as well as the walls of the electronics portion of the sensor head are a minimum of 0.35″ thick aluminum as mandated by the RBSP mission. The mission provided adequate mass allowance that we were not forced to trade weight-relief against the 0.35″ requirement. All aluminum housing pieces are passivated with a chromate conversion coating and all joints are staggered to provide a seal against electro-magnetic emissions.

3.10 Analog Electronics

Each of the two Analog PWBAs in the electronics box contains five identical analog chains (see Fig. 13) comprising three sections: (1) A fast-channel discriminator performs threshold testing, initiates timing to sample the slow-channel peak, and provides a means to evaluate detector coincidence and pile-up conditions, (2) A slow-channel pseudo-Gaussian shaper creates a pulse whose amplitude is proportional to the charge deposited in the detector. (3) A high-speed ADC provides pulse height measurement of the slow-channel peak.

3.11 Fast-Channel

As mentioned earlier, the time from the inflection point on the CSA waveform to full charge collection is consistently 170 ± 20 ns. This relationship propagates through the slow channel semi-Gaussian shaper so that its peaking occurs at a similarly repeatable time relative to the CSA signal inflection point. The fast-channel discriminator therefore marks the CSA inflection point as a fiducial for FPGA event timing. Figures 14 and 15 illustrate how the fast and slow channel signals are collected for event timing and acquisition.

The fast channel incorporates a double-differentiator, and a zero-crossing discriminator with hysteresis. As implemented, the discriminator triggers (at a threshold that is adjustable) on the leading edge of the initial d^2V/dt^2 excursion and the comparator hysteresis holds-off de-assertion until the subsequent zero crossing. As a consequence the trigger pulse duration varies from 50 ns to 160 ns but the trailing edge of the pulse to full charge collection is relatively constant.

The threshold for each channel's discriminator is adjustable to accommodate variations in CSA gains and increased noise in the detectors from radiation damage. The threshold adjustment range is from about 300–1100 keV (Si) in ∼50 keV (Si) increments.

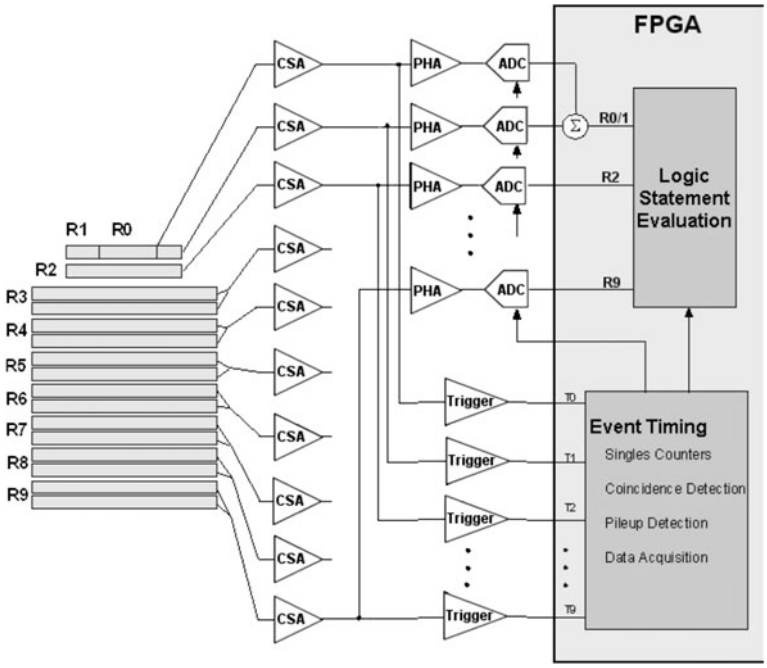

Fig. 14 Slow and fast channel signal flow. The FPGA coordinates slow channel particle event collection based on fast channel timing

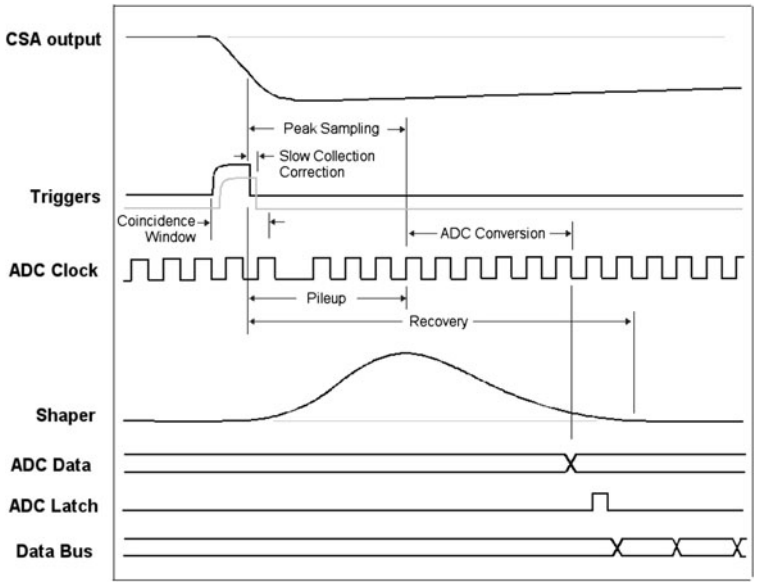

Fig. 15 Particle event timing and data acquisition. *Bold traces* show nominal charge collection and resulting timing events. The *lighter traces* illustrate slow charge collection with the associated timing based correction

3.12 Slow-Channel

The slow channel pulse shaping time is a compromise between long peaking times to minimize ballistic deficit and faster peaking times to support the high-flux environments (Baker et al. 2008). With the measured charge collection times, a 5th order pseudo-Gaussian shaper design was selected with a peaking time on the order of 650 ns (Gornov et al. 2002) and a gain of 60 mV/MeV (Si) with ballistic deficit losses less than 3 % (Loo et al. 1988). The design utilizes methods (Mosher 1976; Beche 2002) for excellent baseline recovery and is implemented with a 4-pole Sallen-Key low pass filter using a low-power, 100 MHz, op-amp. The first stage of the shaper includes a pole-zero cancellation network to compensate for the CSA pole.

The AC coupling of the CSA signal makes the slow channel susceptible to baseline drift, particularly during high flux periods. To correct for this a gated-baseline restore circuit is included which integrates the shaper output between particle events and subtracts that from the shaper input.

3.13 Timing, Coincidence and Pile-up

Using the trigger pulses from the fast channel discriminators, the FPGA based algorithms perform various qualification- and acquisition-related timing functions. In the typical case, triggers from one or more detectors go high and then low within a coincidence window of 250 ns indicating that a single coherent event occurred. When the first of the triggers de-asserts and falls the FPGA adjusts the global ADC sample clock so that a sample edge will occur 475 ns from the trigger trailing edge, to coincide with the slow channel peaking time. From that trailing edge the FPGA also times each of the other trigger trailing edges, so as to apply a mis-sampling correction factor for slow charge collection, as discussed earlier. From the trailing edge of the last trigger to de-assert the FPGA starts a 1000 ns deadtime timer during which the slow channels will be peaking and recovering.

As pile-ups are a critical product of these timing functions, the FPGA detects three classes of pile-up events in the slow channels: immediate pile-up, where a trigger pulse extends outside the coincidence window, primary pile-up where a subsequent particle causes a trigger before a preceding event has been sampled by the ADCs, and secondary pile-up where a second event happens after a preceding event has been sampled but close enough that the second event is riding on the tail of the first. At higher fluxes the separate smaller active areas, R0 and R1, on the front detector provide improved pile-up detection. The FPGA produces a count of all pile-up events but does not sample or analyze them.

Correction of the slow charge collection from shallow penetrating ions is another timing based function carried out by the FPGA. Using the number of 25 ns FPGA clock cycles from the first trigger from a stack event to the each subsequent trigger as indices to a lookup table of multiplication (MLUT) correction factors, the measured energy values are corrected for sampling off of the waveform peak.

3.14 Pulse Height Analysis

The sampling of the slow channel pseudo-Gaussian shaped pulse is carried out by the 12-bit ADC operating at 10 MHz. Input offset and scaling to the ADC is selected such that a 0 MeV (Si) input produces an output of $\sim$20 DN (digital number) and gain is 37 DN/MeV.

The FPGA can shift the ADC clock with 25 ns resolution so as to align the sampling edge with the peak of the slow channel pseudo-Gaussian pulse. The 25 ns resolution arises from the FPGA 40 MHz operation and corresponds to $<$1 % amplitude error from sampling off the waveform peak.

Table 2 Electron energy bin logic statement parameters

No.	ΔE (MeV)	Logic condition (energy equation)[a]
1	1.6–2.0	$(R_1 \geq 0.4) \cdot (R_2 \geq 0.4) \cdot (R_{12} \leq 1.35) \cdot \bar{R}_{39}$
2	2.0–2.5	$(R_1 \geq 0.4) \cdot (R_2 \geq 0.4) \cdot (1.3 \leq R_{12} \leq 1.7) \cdot \bar{R}_{39}$
3	2.5–3.2	$(R_{12} \geq 0.8) \cdot (1.85 \leq R_{13} \leq 2.25) \cdot \bar{R}_{49}$
4	3.2–4.0	$(R_{12} \geq 0.4) \cdot (2.65 \leq R_{13} \leq 2.95) \cdot \bar{R}_{49}$
5	4.0–5.0	$(R_1 \geq 0.4) \cdot (R_{23} \cdot 0.4) \cdot (3.35 \leq R_{14} \leq 3.95) \cdot \bar{R}_{59}$
6	5.0–6.2	$(R_1 \geq 0.4) \cdot (R_{24} \cdot 0.4) \cdot (4.4 \leq R_{15} \leq 5.0) \cdot \bar{R}_{69}$
7	6.2–7.7	$(0.4 \leq R_1 \leq 1.0) \cdot (0.4 \leq R_{2\_} \leq 2.0) \cdot (R_{34}\_0.4) \cdot (5.5 \leq R_{15} \leq 6.25) \cdot \bar{R}_{69}$
8	7.7–9.7	$(R_1 \geq 0.4) \cdot (0.4 \leq R_{2\_} \leq 1.0) \cdot (R_{34} \geq 2.4) \cdot (5.75 \leq R_{36} \leq 6.6) \cdot \bar{R}_{79}$
9	9.7–12.1	$(R_1 \geq 0.4) \cdot (0.4 \leq R_{2\_} \leq 1.0) \cdot (0.4 \leq R_3 \leq 2.0) \cdot (R_4 \geq 0.4) \cdot (R_{56} \geq 0.4) \cdot (8.0 \leq R_{37} \leq 9.0) \cdot \bar{R}_{89}$
10	12.1–15.1	$(R_1 \geq 0.4) \cdot (R_2 \geq 0.4) \cdot (R_3 \geq 0.4) \cdot (R_4 \geq 0.4) \cdot (R_5 \geq 0.4) \cdot (R_6 \geq 0.4) \cdot (R_7 \geq 0.4) \cdot (10.3 \leq R_{38} \leq 12.5) \cdot (R_9 \leq 0.4)$
11	15.1–18.9	$(0.4 \leq R_1 \leq 1.0) \cdot (R_2 \geq 0.4) \cdot (R_3 \geq 0.4) \cdot (R_{48} \geq 0.4) \cdot (R_{59} \geq 11.0)$
12	18.9–	$(0.4 \leq R1 \leq 1.0) \cdot (0.4 \leq R_2 \leq 1.0) \cdot (0.4 \leq R_3 \leq 1.5) \cdot (R_{48} \geq 0.4) \cdot (R_{59} \geq 15.0)$

[a] $R_{xy} = R_x + R_{x+1} \ldots R_y$
$\bar{R}_{xy} = (R_x < 0.4) \cdot (R_{x+1} < 0.4) \cdot (\cdots) \cdot (R_y < 0.4)$

3.15 Event Processing

The process of classifying particle events by type and energy range proceeds by comparing the PHA data from individual detectors and PHA sums of select detectors against sets of energy bounds, with each set defining an energy bin. The energy bound conditions are written as logic statements with multiple terms that if all evaluate as true the count of the energy bin for that particle type is incremented. The general form of the logic statements is shown below where $\prod$ and $\cdot$ are logical 'And' operators and the δ operator signifies inclusion.

$$E_+ = \prod_{i=1}^{9} (E_{lo_i} \leq R_i \leq E_{hi_i}) \cdot \left(E_{lo_A} \leq \sum_{i=0}^{9} \delta_{A_i} \cdot R_i \leq E_{hi_A} \right) \cdot \left(E_{lo_B} \leq \sum_{i=0}^{9} \delta_{B_i} \cdot R_i \leq E_{hi_B} \right) \tag{3}$$

Each logic statement has up to nine terms comparing each detector PHA against low and high bounds, and two terms where summations of included detector values are compared against low and high bounds.

The specific limits for each of the 12 electron and 8 proton energy bin logic statements are given in Tables 2 and Table 3, respectively.

The diagram in Fig. 16 shows PHA signal flow through the FPGA for particle event processing. On the left, the raw PHA values are adjusted to a zero offset common DN/MeV scale using the MLUT and GCO tables described below; then the results from the separate active areas of the front detector are summed. The scaled PHA values are held in registers where they are gated sequentially into the evaluation circuitry as the various energy bin bounds are also presented. For any given energy bin logic statement, the bounds are evaluated until a term fails or all evaluate true. The result is then noted and the process repeats for the rest of the bins. Because a particle event is evaluated for all bins, a particle can match one

Table 3 Proton energy bin logic statement parameters

No.	ΔE (MeV)	Logic condition (energy equation)[a]
1	18.5–24.0	$(R_1 > 8.0) \cdot (R_2 > 6.8) \cdot \bar{R}_{39}$
2	24.0–31.2	$(R_1 > 0.5) \cdot (R_2 > 5.0) \cdot (R_3 > 11.0) \cdot \bar{R}_{49}$
3	31.2–40.6	$(R_1 > 0.5) \cdot (R_2 > 0.5) \cdot (R_3 > 10.0) \cdot (R_4 > 13.2) \cdot \bar{R}_{59}$
4	40.6–52.8	$(0.5 < R_1 < 4.7) \cdot (0.5 < R_2 < 6.0) \cdot (R_3 > 0.5) \cdot (11.5 < R_{46} < 33.0) \cdot \bar{R}_{79}$
5	52.8–68.6	$(0.5 < R_1 < 5.5) \cdot (0.5 < R_2 < 6.5) \cdot (R_3 > 0.5) \cdot (R_4 > 0.5) \cdot (R_5 > 0.5) \cdot (3.0 < R_{68} < 40.0) \cdot (R_9 < 1.5)$
6	68.6–89.2	$(0.5 < R_1 < 5.0) \cdot (0.5 < R_2 < 5.0) \cdot (R_3 > 0.5) \cdot (R_4 > 0.5) \cdot (R_5 > 0.5) \cdot (R_6 > 0.5) \cdot (R_7 > 0.5) \cdot (R_8 > 0.5) \cdot (37.0 < R_{18} < 65.0) \cdot (R_9 > 0.5)$
7	89.2–116.0	$(0.5 < R_1 < 3.0) \cdot (0.5 < R_2 < 3.0) \cdot (3.0 < R_3 < 5.5) \cdot (3.0 < R_4 < 7.0) \cdot (3.0 < R_5 < 6.0) \cdot (3.0 < R_7 < 6.0) \cdot (4.5 < R_8 < 7.0) \cdot (31.0 < R_{19} < 45.0)$
8	116.0–	$(0.5 < R_1 < 5.0) \cdot (0.5 < R_2 < 5.0) \cdot (5.0 < R_{18} < 28.0)$

[a] $R_{xy} = R_x + R_{x+1} \ldots R_y$
$\bar{R}_{xy} = (R_x < 0.5) \cdot (R_{x+1} < 0.5) \cdot (\cdots) \cdot (R_y < 0.5)$

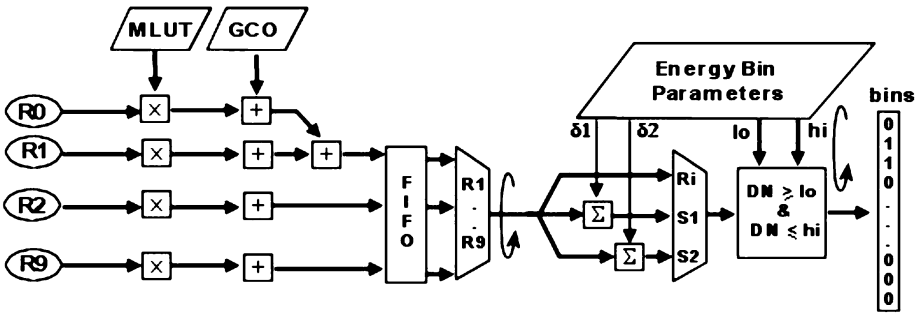

Fig. 16 Data flow in energy bin logic statement evaluation. Detector PHA values are adjusted to a 0 offset common DN/MeV scale and then sequentially compared to the energy bounds of each energy bin logic statement. The results are passed to the FPGA science telemetry block

or more bins; in this case, all matching bins will be tallied. The binning results are passed on to the spin sectoring section of the FPGA. If a particle does not fall into any bin, it is incremented into a 'no-match' counter.

For evaluation by the FPGA, the logic statement bounds and detector PHA values must have the same DN/MeV scale. Although each detector channel was designed to have a nominal gain of 37 DN/MeV and 20 DN offset, variations were unavoidable. To accommodate these variations and any changes that may develop over time, the FPGA uses the MLUT (multiplication lookup table) for channel-by-channel gain normalization and the GCO (gain correcting offset) table to produce zero offset values.

The MLUT contains gain correction terms for each channel convolved with the correction terms for slow charge collection. Using the channel number and any measured trigger delay as indices to the lookup table, the returned value effects both corrections to the PHA values with a single multiplication operation. The values returned by the GCO lookup table are the negative of each channel's characteristic offset. Subtracting them from the PHA produces a zero-offset value.

Due to limitations imposed by the implementation of the MLUT, each REPT instrument has a slightly different optimum common DN/MeV scale. As a consequence the DN values of the energy bin limits must be scaled for each instrument to match. Each instrument's tables of offset, gain and scaled logic bounds are uploaded from the ground each time the instruments are power cycled.

REPT science data collection is synchronized with the spacecraft spin period; each spin is subdivided into 36 equal duration sectors. The FPGA gets the spin period and phase once a second from the spacecraft and interpolates between updates with internal counters. If the internal counters become out of sync with the spacecraft, the FPGA will advance its internal sector counter until it is once again in sync with the spacecraft, flagging the data for each sector with an error. In cases such as spacecraft eclipses where the spin period and phase information are flagged by the spacecraft as invalid, the REPT FPGA propagates its internal sector counters from the last known good spin period and phase information and resynchronizes as described above when the spacecraft indicates the provided spin period and phase data are once again valid.

3.16 Digital Board

The Digital PWBA carries the REPT system FPGA, the spacecraft communications drivers, and the instrument housekeeping collection system. The FPGA is an Actel RTAX2000S operating at 40 MHz. In addition to particle event processing the FPGA handles commanding, collects housekeeping data, and formats and sends telemetry packets to the spacecraft. The details of the FPGA design and operation are given later in the FPGA section.

3.17 Power Supply

The REPT Power PWBA is a custom-built pulse width modulated (PWM) DC-DC power converter using a single-switch, current-mode control, forward converter topology to generate 3.3 V and ±5 V. The 3.3 V secondary is regulated using a discreet magnetic feedback circuit to bridge the isolation barrier. The ±5 V secondaries rely on a coupled inductor to provide cross-regulation. Additional lower voltages, 2.5 V for ADCs and 1.5 V for the FPGA core, are generated using linear regulators powered by the 3.3 V primary and providing better than 1 % regulation.

A second output on the PWM is used to drive the 320 V bias generation. The PWM output is AC coupled to a step-up transformer with the secondary driving a 4-stage series voltage multiplier. The output of the voltage multiplier is series regulated to 320 V and designed to provide ∼500 μA to the Bias & CSA PWBA supporting the worst case end-of-life radiation and elevated temperature.

3.18 Thermal

The REPT instrument, as shown in Fig. 17, utilizes a passive thermal design. It is thermally isolated from the RBSP spacecraft with G-10 spacers and titanium bolts. Multi-layer insulation (MLI) blankets around the electronics box decouple it from the spacecraft interior while radiator surfaces across the sensor housing allow for cooler operating temperatures. The radiator surfaces consist of Germanium Black Kapton sheets attached with an electrically conductive adhesive. The MLI blankets consist of an electrically conductive outer layer of 100XC black Kapton and typical aluminized Kapton inner layers. A single survival heater circuit with series-redundant thermostats maintains REPT temperatures when the instrument

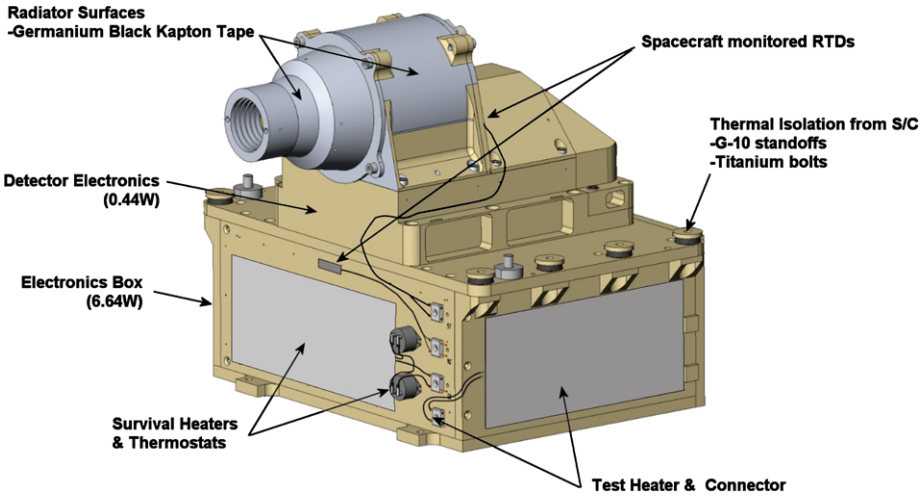

Fig. 17 REPT Thermal Systems. Thermal standoffs and MLI blankets (not shown) isolate the instrument from the spacecraft deck while radiator tape on the sensor head provides a −1 °C nominal detector temperatures

is powered off. Both survival and the test heater elements are a specific magnetically cancelling design. The REPT temperature is monitored through several internal housekeeping thermistors, plus two spacecraft-monitored platinum thermal sensors.

The predicted on-orbit temperatures are: −21 °C to +22 °C for the sensor head with the -1 ± 10 °C being the most likely, and −17 °C to +28 °C for the electronics box with a most likely prediction of $+6 \pm 11$ °C. Variation over any given orbit is expected to be on the order of 1–2 °C. The wide ranges are due to unknowns in the spacecraft operating temperatures.

3.19 Magnetic Compatibility

REPT performance is not affected by spacecraft magnetic fields. The REPT design has been fully reviewed and is compliant with the rigorous RBSP mission magnetic cleanliness requirements, so as to not impact the EMFISIS Search Coil or Magnetometer. All materials were screened for minimal magnetic remanence. For the few cases where the use of non-ideal materials were required, the materials were de-gaussed, tracked, and reported to the mission. All high current paths in the instrument were identified and reviewed. The layout of the electronics PWBA considered low frequency DC current paths to reduce the magnetic loop area. The survival heaters, and the wiring to them, were specially selected and routed to be magnetic-cancelling in the far field.

3.20 Telemetry

REPT telemetry consists of science (energy bins, PHA, space weather), engineering (housekeeping, calibration results) and command responses. The full set of telemetry packets is shown in Table 4. All telemetry is formed in CCSDS packets of less than 256 bytes.

The primary science data, reported in the "Science" packet, consists of particle energy spectral data collected for each of the 36 spin sectors and reported to the spacecraft once each spin. It consists of counts of particle events classified into each of the 20 energy bins, particles not able to be classified, pileup events and counts of triggers on each detector. The

Table 4 REPT telemetry items

Packet name	APID	Size (bytes)	Default RUN rate	Default SAFE rate	Contents
Instrument housekeeping	$0 \times 20A$	80	1/min	1/s	General health and safety info
Critical housekeeping	0×200	18	1/s	1/s	Health and safety info monitored by Mission Operations Center
Space weather	0×201	18	1/spin	None	Real-time space weather info
Science	0×202	1820	1/spin	None	All equations and singles counts
Pulse height analysis (PHA)	0×205	1622	1/50 s	None	Raw signal information
Calibration	0×206	1320	On Cmd	On Cmd	Results of charge injection
Command echo	0×207	14	On Cmd	On Cmd	Opcode and result of last command
Memory read	0×208	254	On Cmd	On Cmd	Memory dump
Checksum	0×209	20	On Cmd	On Cmd	Result of checksum command

data are marked with the instrument ID, Mission Elapse Time (MET) at start of the spin and end of each sector, whether the instrument identifies any potential errors in the sector timing, the state of the bias voltage, and the version of the particle classification logic equations. All counting data are collected in 23 bit counters and reported in an 8 bit mantissa, 4 bit exponent pseudo-log compression providing a dynamic range of over 8 million with less than 1 % loss.

The secondary science data, "PHA," provides a sampling of the collected pulse-height analysis data. Each packet consists of 100 PHA data sets where each PHA set is generated by a particle event and contains 10 bit ADC values for each detector, as well as the energy bin(s) matched by these values. The PHA data are only generated by events that meet validity (timing and coincidence) requirements. The PHA science data are collected at a configurable cadence, with once every 12 ms being the fastest and 500 ms being nominal for flight.

For space weather, the third science data packet, REPT reports the singles counts on detectors R2, R4, and R9, over full spins (all 36 sector counts are combined). These detector single counts correspond roughly with electrons of 2, 5, 10 MeV and protons of 20, 50, 70 MeV.

Housekeeping packets contain information about the state of health of the instrument. REPT has two housekeeping packets, Instrument Housekeeping and Critical Housekeeping. Instrument Housekeeping is a comprehensive set of data points. It contains operating states, packet rates and status, command success/failure counts and codes, other error counters, temperature values from around the instrument, and power supply voltage and current monitors including detector leakage currents. It is typically sent once per second while in SAFE mode, and once per minute when in RUN mode. The Critical Housekeeping packet is a small subset of these data points and is given priority handling both by the spacecraft and by the Mission Operations Center (MOC) as it is among the first data sent down by the spacecraft upon contact with the ground and when received by the MOC its contains will be checked against a set of limits and alarms emailed out as appropriate.

The remaining telemetry packet types are those issued by the instrument in response to a command. The calibration telemetry packet contains the 100 PHA sets resulting from a cali-

Table 5 REPT commands

Command name	Opcode	Description
NOOP	3	No operation
ARM	6	Enter ARM state to allow protected commands
RUN	9	Enter RUN mode
SAFE	12	Enter SAFE mode
CALIBRATE	15	Issue a calibration packet
BIAS_ON	18	Turn on BIAS voltage (Protected)
BIAS_OFF	21	Turn off BIAS voltage
MEM_READ	24	Read FPGA registers/memory
MEM_WRITE	27	Modify FPGA registers/memory
CHECKSUM	30	Request a checksum over a portion of FPGA memory

bration command as described previously, along with a record of the commanded calibration level and analog measurements verifying the actual level.

The telemetry responses to the Checksum and Memory Read commands are discussed below in commanding. The remaining command response packet, Command Echo, is used for communication and commanding diagnostics. When enabled, it repeats each command received back to the ground along with a success/fail indictor. The issuance of the Command Echo response is controlled by writing to a FPGA memory register and is disabled by default.

The total telemetry allocation for REPT is 1580 bits per second. Of this, primary energy bin science uses about 78 %, instrument housekeeping takes up 1 %, and secondary PHA science uses the remaining 21 % but is periodically adjusted down to 17 % to accommodate internal calibration data.

3.21 Commanding

The REPT command set is relatively small. The full set is given in Table 5. Without a microprocessor, commanding of REPT largely entails writing to configuration registers in the FPGA. The registers of particular interest are the following:

- Energy Bin parameters: These registers contain the parameters used for the twenty energy bin logic statements. There is also a separate register that contains the current version of the parameter set.
- Data Processing Registers: These are the registers that contain the GCO and MLUT tables, used to normalize the calibration of each analog chain. There are also separate registers that contain the current GCO and MLUT version.
- Acquisition registers: These registers describe the requirements for valid events, including required triggers, coincidence window duration and timing restrictions.
- Threshold Registers: These registers are used to adjust the trigger sensitivity of each of the detectors.

There is an assortment of other registers for enabling and setting the cadence of telemetry transmission, resetting errors counters and low-level diagnostics. All FPGA registers are configured through the MEM_WRITE command. Each MEM_WRITE command can configure up to 40 separate register addresses. Likewise the MEM_READ command can

request the contents of up to 40 separate registers, which will be reported in the Memory Read telemetry packet.

Aside from the Memory Read/Write commands there are seven explicit commands to the REPT instrument. These are CALIBRATE, NOOP, ARM, SAFE, RUN, BIAS_ON, BIAS_OFF, and CHECKSUM. The CALIBRATE command is discussed above in regard to its operation and telemetry. The NOOP command is the generic null operation that does no action except increment the command success counter and issue an echo packet (if enabled). The SAFE and RUN commands are used to set the REPT operating mode. The CHECKSUM command calculates a CRC checksum over a selected range of memory registers. It is used to verify the integrity of the GCO, MLUT and Energy Bin parameter tables. The calculated checksum comes to the ground in its own telemetry packet.

The ARM command allows the FPGA to accept an immediately subsequent BIAS_ON command which enables the bias voltage supply. The 320 V bias supply poses a risk to personnel and, in some situations, the instrument itself so is protected from being inadvertently enabled. The BIAS_OFF command removes power from the bias supply voltage. It is not protected and can be sent at any time.

4 Instrument Testing, Characterization, and Calibration

REPT calibration was done both at the each individual detector level as well as the instrument level at accelerator beams. For the latter calibration both the flight models as well as the engineering model were calibrated at electron and proton facilities. The details of the calibration are given below.

Each detector comprising both the REPT stacks was calibrated using a trinuclide alpha source in vacuum as well as charge injection to establish the ADC to MeV relationship. Figure 18 shows the ADC counts (DN) as a function of the injected charge for a pair 40 mm detectors comprising the 8th element of one of the flight models of REPT together with a straight line fit to the data. It is clear from the figure that there is excellent linearity between the energy loss and the ADC counts over the entire range of expected energy loss for electrons and protons. Furthermore, the trinuclide alpha source with emitted alpha energies of 5.15, 5.48, and 5.80 MeV lie on the fit straight line further confirming and establishing the ADC to MeV conversion. The number of points scattered along the bottom of the graph

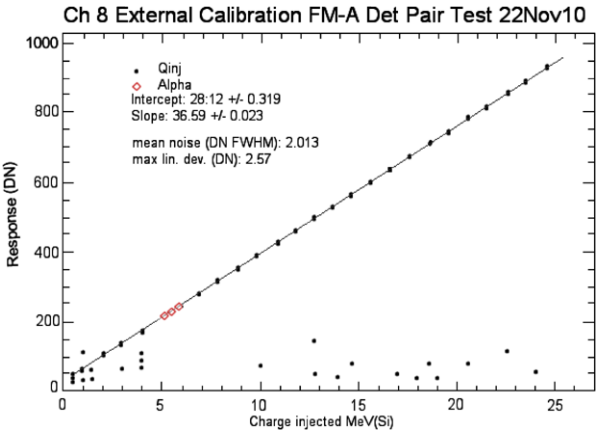

Fig. 18 External charge injection calibration

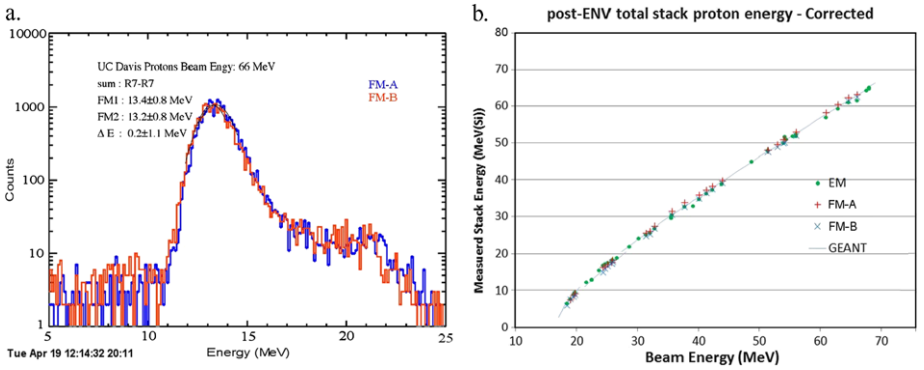

Fig. 19 (**a**) Energy deposited in R7 by 66 MeV protons in R7. The *red* and *blue curves* are for FM-A and FM-B respectively; (**b**) the total energy deposited in the detector stack as a function of the incident proton energy. Proton beam measurements for FM-A, FM-B, EM are shown as *symbols*. Expected total energy from GEANT4 simulations are superposed as a *solid line*

are due to the test setup. The signals from the sensor head were passed through the vacuum chamber wall to the electronics box situated outside.

The offsets and the slopes for all nine channels for each sensor are implemented in the FPGA as an offset and multiplication lookup tables. Each REPT sensor also has an internal calibration circuit to track changes in gain and offset over the period of the mission. This calibration tracking, which takes ∼5 minutes, will be performed periodically to ensure measurement integrity. Sensitivity to threshold changes was also investigated using charge injection. Maximum allowable thresholds accounting for detector/electronics noise were established to be less than 0.365 MeV, which is below the differential channel logic equation threshold of 0.4 MeV. The calibration results were in accordance with GEANT4 simulations, which showed that varying the threshold from 0.35 to 0.41 MeV did not significantly affect singles efficiencies; particularly for the front detector, which is used to trigger pulse height analysis.

The two flight units, FM-A and FM-B, as well as the engineering model (EM), were calibrated and tested at proton and electron accelerators. Calibrations included individual detector response as well as the total stack response and validating differential channel efficiencies. Figure 19a shows the comparison of energy loss in the R7 detector between FM-A and FM-B for an incident proton beam of 66 MeV. The instruments were mounted on a movable platform and exposed sequentially to the beam as it was maintained at the same tune. Figure 19a shows near identical energy response of detector element R7 in both FM-A and FM-B. The mean positions as well as the deposition profiles are in excellent agreement with each other.

Figure 19b shows the summed energy from the entire detector stack as a function of the incident proton energy for all the three instruments as well as the GEANT4 predicted response. The former are shown as symbols and the latter as a solid line. The individual detector pair gains had to be corrected with a factor that varied from 0 to 3 %. This correction factor was obtained from examining proton punch through for the detectors and is included in the energy sums shown in Fig. 19b. The corresponding results for electrons are shown in Figs. 20a and 20b. The former shows the energy deposited in the second detector, R2 of the stack for incident electrons of 10.6 MeV in energy with the red and blue histograms corresponding to FM-B and FM-A respectively. Also shown are Gaussian fits to the primary

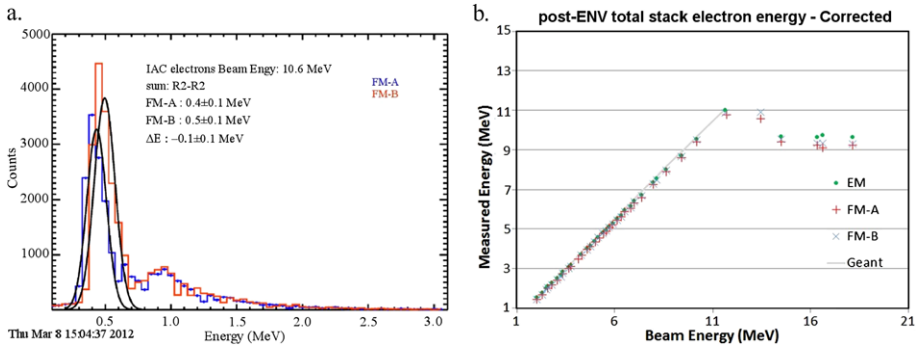

Fig. 20 (**a**) Energy deposited in R2 by 10.6 MeV electrons in R2. The *blue* and *red histograms* are for FM-A and FM-B respectively. The secondary peak to the right is due to 2 electrons per beam pulse (**b**) the total energy deposited in the detector stack as a function of the incident electron energy. Electron beam measurements for FM-A, FM-B, EM are shown as *symbols*. Expected total energy from GEANT4 simulations are superposed as a *solid line*

peak, with the mean and standard deviation indicated in the figure. There is excellent agreement between the two instruments for energy loss in individual detectors (other detectors show similar pattern to that of R2). The smaller peak to the right in Fig. 20a is due to pileup (2 electrons per pulse) from the accelerator beam.

Figure 20b shows the total energy seen in the entire detector stack as a function of the incident electron beam energy. The symbols represent measurements by the EM, FM-A and FM-B units while the solid line is the expected energy according to GEANT4 simulations. The measurements by each of the instruments and GEANT4 predictions are in close agreement. At beam energies from about 10 to 12 MeV, there is a small discrepancy between GEANT4 and measurements, most likely due to not accurately determining beam energy arising from difficulties in tuning the beam with single electron per pulse. Figure 20b also shows that beyond about 12 MeV, most electrons penetrate the full stack and the stack energy is independent of the incident beam. However, due to the fact that electrons straggle, REPT is able to measure electrons differentially up to nearly 20 MeV (see below).

As mentioned before (Sect. 3) REPT measures electrons in 11 differential channels and 1 integral channel and protons in 8 differential channels. The differential channels are obtained using logic conditions (equations) on energy deposits in individual detectors as well as summed energies on specific sets of detectors. GEANT4 simulations were used to determine these equations and all of the three REPT units were calibrated at proton and electron beams. As previously mentioned, Tables 2 and 3 show the logic conditions for electron and proton differential channels.

The logic conditions for electrons and protons yield efficiencies as a function of incident particle energy which are used to obtain particle spectra. The shapes and amplitudes of the channel efficiencies can then be validated at particle accelerators. As noted, all three instruments were calibrated at electron and proton beams. Figures 21a and 21b show the results of beam calibrations for electrons and GEANT4 predicted efficiencies, respectively.

The measured and the calculated efficiencies agree closely both in functional form and in amplitude. The EM, FM-A and FM-B are in good agreement with one another and the small differences arise mainly from lack of absolute counts from the LINAC. Note that for the differential channel measurements, the LINAC had to be operated in dark current mode due to the requirement of a single electron per beam pulse.

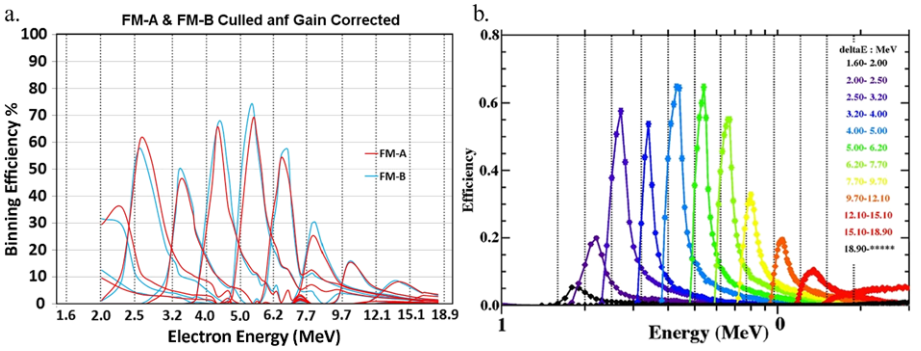

Fig. 21 Electron differential channel efficiencies (**a**) measured and (**b**) GEANT4 simulated. The three REPT units, EM, FM-A and FM-B are shown as *green*, *red* and *blue traces* respectively in panel (**a**). The nominal differential channel energies are indicated in panel (**b**) to the right, which shows GEANT4 efficiencies as different color-coded traces

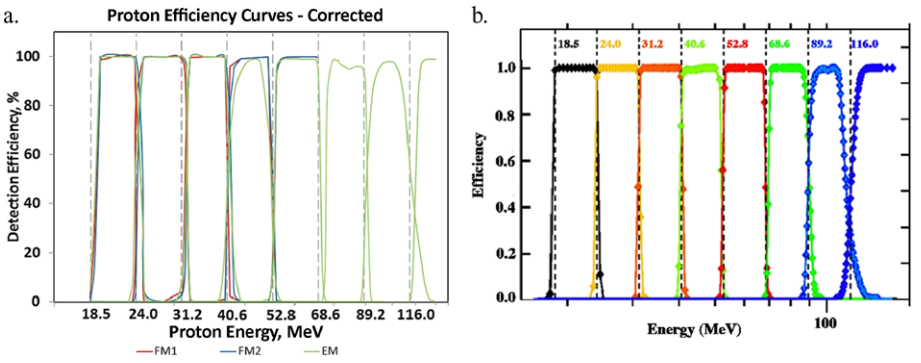

Fig. 22 Proton differential channel efficiencies (**a**) measured and (**b**) GEANT4 simulated. The three REPT units, EM, FM-A and FM-B are shown as *green*, *red* and *blue traces* respectively in panel (**a**). All the channels were not measured at the same beam (see text for details). The nominal differential channel energies are indicated in panel (**b**) to the right that shows GEANT4 efficiencies as different color coded traces

Figure 22 shows the differential channels for protons. As noted for the prior figure, Fig. 22a shows measured efficiencies (at proton beams) and Fig. 22b shows the GEANT4 calculations. The proton channels resemble step functions and are seen to be nearly identical among the three instruments and agree closely with GEANT4 simulations. The two flight models were not exposed to the highest beam energies to limit exposure to radiation and given close agreement with GEANT4 results for the lower energy channels.

It is crucial that REPT be able to measure electrons in the presence of protons, for slot filling (extreme) events that can overlap with the inner belt. To ensure this, we tested the engineering model with a Sr90 source in the 200 MeV beam at the Indiana University proton accelerator. Figure 23 shows the results, with the top histogram showing the combined energy deposit in the front detector and the red trace the Sr90 signal after removing the protons using the expected proton response in the second detector. For comparison, the expected signal for Sr90 alone is shown as a blue trace. It is clear that the electron signal from Sr90 can be separated over backgrounds of less than about 2 %. This accuracy is expected to improve much more for the differential channels as signal from multiple detectors are combined to

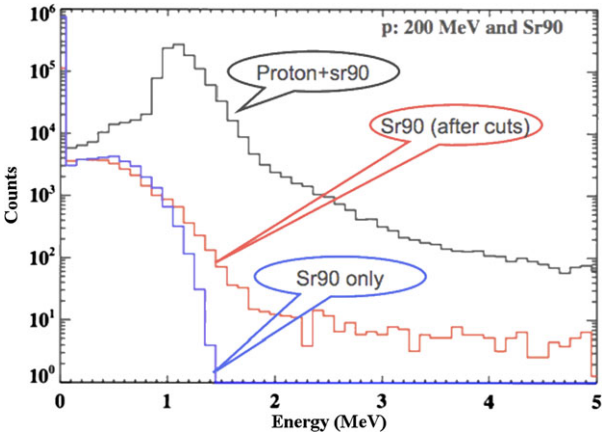

Fig. 23 Separation of electrons and protons in REPT. The histograms show energy deposited in the front detector for (**a**) combined Sr90 and 200 MeV protons (**b**) Sr90 signal over negligible background after removing protons using expected proton response and (**c**) for a purely Sr90 source

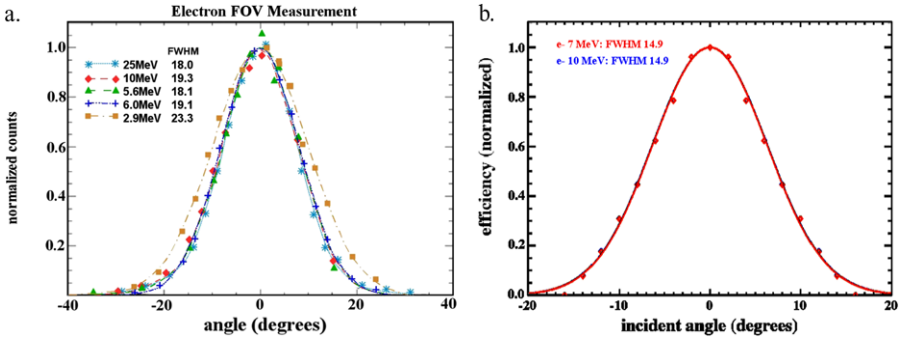

Fig. 24 Angular response of REPT (**a**) at electron beam tests and (**b**) as determined by GEANT4. The response at test beam was measured over a range of energies indicated in (**a**) and at 7.0 and 10.0 MeV for GEANT4

identify electrons. While it is not possible to obtain electrons and protons simultaneously at all energies, we have verified using GEANT4, the ability of REPT to cleanly separate electrons and protons under almost all circumstances.

The REPT field of view set by the collimator determines the geometry factor and therefore the count rates observed. We have measured the field of view for both protons and electrons at test beams and compared to the design set by GEANT4 simulations.

Figures 24a and 24b show the field-of-view for electrons as determined at test beam and GEANT4 simulations, respectively. The measured FWHM is slightly larger than the simulations indicate. This is due to multiple scattering of electrons in air over approximately 2 m-distance that separated the instruments from the beam port (note the FWHM measured at the lowest energy of 2.9 MeV is the highest as expected due to scattering).

In order to minimize background due to side penetrating particles REPT was designed with aluminum-tungsten shielding. The detection efficiencies for both protons and electrons impinging perpendicularly on the instrument were measured in test beams.

Figure 25a shows the measured efficiencies for detectors R3 and R4 with the latter multiplied by a factor of 0.1 to clearly separate the curves. Efficiencies for the two smaller front detectors were also measured (not shown) and were found to be in agreement with GEANT4 results. Due to uncertainty in determining the incident electron flux, the measured efficien-

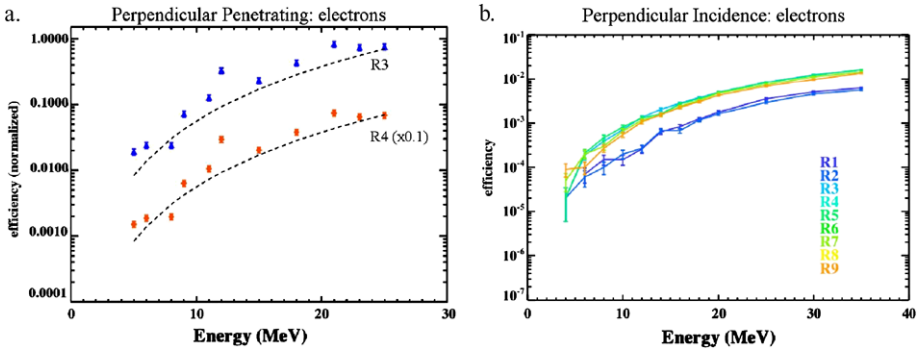

Fig. 25 (**a**) Efficiency of counting side-penetrating electrons in REPT for Detector R3 (*blue*) and Detector R4 (*red*); (**b**) Similar to (**a**) for all detectors in REPT stack and perpendicular (90°) electron incidences

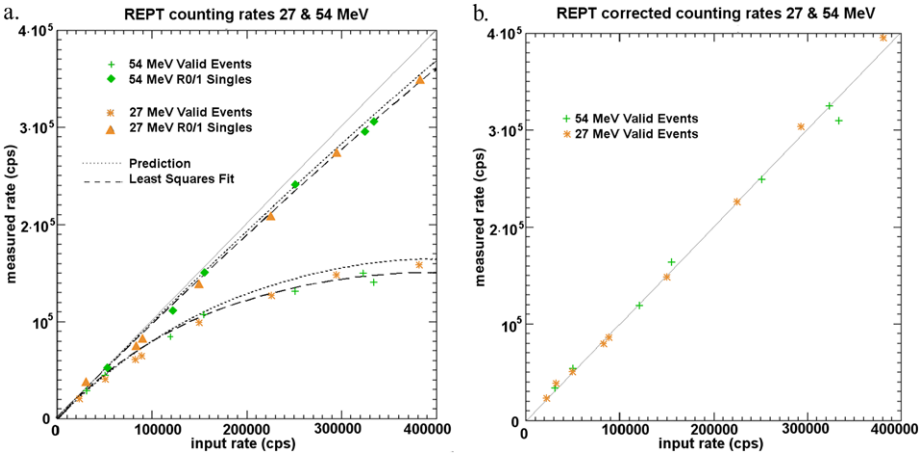

Fig. 26 (**a**) Well-behaved counting rate and dead time performance supports (**b**) excellent dead time correction factor determination

cies are shown normalized with the efficiency set arbitrarily to unity for beam energy of 25 MeV. Figure 25b shows efficiencies for all detectors (color coded as indicated in the figure) as determined by GEANT4. These efficiencies are absolute and were used to estimate background due to side-penetrating electrons. Note that as expected the efficiencies for the two front detectors are systematically less than the rest of the stack since the front detectors are smaller. Most importantly, the functional form of the measured and the GEANT4 efficiencies are in excellent agreement thereby confirming the use of GEANT4 both for design and background estimation aspects.

The proton side penetrating efficiency has a simple step function-like behavior with an efficiency of unity for protons greater than 110 MeV and zero for all energies below. This behavior was confirmed at proton test beam as well.

As described earlier, the division of the front detector into two active areas, coupled with the deterministic timing characteristics of the fast channels, supports excellent counting rate determination. The plot in Fig. 26a shows REPT reported R0/1 singles and valid event (i.e., pile-up free) rates for proton event rates of 0 to >300000 per second for both 27 and 54 MeV

protons. Also included are the plots for predicted singles rates and pile-up free (valid) events rates. The recorded performance is very close to predictions particularly for singles rates.

The REPT slow channels are best considered as paralyzable systems where actual counts m are related to the measured, essentially pile-up free counts n by

$$m = A_m \cdot n \cdot e^{2 \cdot n \cdot \tau_m} \tag{4}$$

with $\tau_m = 1100$ ns, the slow channel dead time, and A_m is the scaling factor coming from a least squares fit.

However the instrument does not provide a direct count of measured events n, and summing the bins is invalid because individual events can be counted in multiple bins. However, an estimate of n can be derived from the singles counts of the front R0/1 detector plane.

The singles counters are paralyzable as well, but not pile-up free, so the measured R0 + R1 singles rate s is related to the actual rate n by

$$s = A_s \cdot n \cdot e^{n \cdot \tau_s} \tag{5}$$

where τ_s, the fast channel dead time measured in particle beams at ~200 ns, and A_s the scaling factor are given by a least squares fit. This relationship is not directly invertible but the 5 term Taylor expansion of the exponent leads to

$$n = \frac{s}{A_s} \cdot \left[1 + \frac{s}{A_s} \cdot \tau_s + \frac{1}{2} \cdot \left(\frac{s}{A_s} \cdot \tau_s \right)^2 + \frac{1}{6} \cdot \left(\frac{s}{A_s} \cdot \tau_s \right)^3 + \frac{1}{24} \cdot \left(\frac{s}{A_s} \cdot \tau_s \right)^4 + \frac{1}{120} \cdot \left(\frac{s}{A_s} \cdot \tau_s \right)^5 \right] \tag{6}$$

The slow channel dead time correction factor b, based on the estimate of the actual event rate n and the slow channel response rate from Eq. (4), is then given by Eq. (7)

$$b = 1 + \frac{n - m(n)}{m(n)} = \frac{e^{2 \cdot n \cdot \tau_m}}{A_m} \tag{7}$$

The dead time correction must be calculated and applied on a sector by sector basis. Figure 26b shows the valid event data sets with dead time correction factors calculated and applied on a point by point basis. Since n is estimated from the singles rates the error bars remain small.

5 Data Analysis and Data Interpretation

5.1 Data Analysis

The data continuously generated by the REPT instruments will be stored on each satellite until a daily contact with a ground station is made. The data will be then downlinked and stored under the control of the Mission Operation Center (MOC), which will transfer the data to the ECT Science Operation Center (SOC) at the Los Alamos National Laboratory (LANL). These data will be in the form of raw telemetry data, containing both science and housekeeping data used to monitor and maintain REPT. The ECT SOC is responsible for the processing and disseminating the data, which will range from raw telemetry to fully calibrated and validated science data with higher-level products resulting from combined ECT suite-wide data (see Table 6). The processing algorithms and software for REPT will be provided and maintained by the REPT team. The REPT team will also receive and process

Table 6 Descriptions of data levels (Adapted from the ECT_SOC_ICD_01A Handbook, April 29, 2009)

Data level	Description	Availability	Users
L0	Raw de-commutated telemetry data from MOC	Minutes from MOC receipt (Time = T0)	SDC, Archives
L1	L0 + sorted, time-tagged, instrument separated units of count rate. CSCI-1, generated by SOC-CTG	T0+ < 6 hours	SDC, ECT team, archives
L2	L1 + calibrated and corrected (bkg. dead-time, etc.), physical units, CSCI-2, generated by SOC-SDC	T0+ < 1 week Quick-Look T0+ < 1 month Final Release	SDC, Co-Is, GIs, US & Intl scientific community, Other LWS Missions, Archives, Space Weather users, Virtual Observatories
L3	L2 + B-field derived science products (pitch angles, moments, L-sorted), CSCI-2, generated by SOC-SDC	T0+ < 1 week Quick-Look T0+ < 1 month Final Release	
L4	L3 + PSD units derived using B-field models, magnetic coordinates, CSCI-2, generated by SOC-SDC	TO+ < 1 year	

the instrument data from the SOC for the purpose of analyzing the health of the instrument and the quality of the science data.

During normal mission operations, the MOC collects all raw telemetry during contact times and combines these data into a daily MET (Mission Elapsed Time) Level zero (L0) files. The ECT SOC obtains these L0 files as soon as they are available at the MOC, on a roughly daily cadence. The first processing step is to produce Level one (L1) data, daily files in UTC, that contain science data in count rates and state of health (SOH) data in engineering units on standard time tags.

Here we adapt the existing process at LASP for use with the RBSP L0 files, which will be run at the LANL ECT SOC. LASP uses an IDL based process that operates on files of CCSDS packets, and produces output in the form of IDL savesets. Here the inputs are APL MOC L0 files and the agreed output format for ECT is ISTP compliant CDF files.

The first task of the L0 to L1 processing step at the SOC is to strip off the MOC file headers, resulting in a raw CCSDS packet file containing the housekeeping and science data in an unmodified form. The decoding software, developed and provided by LASP, simply separates this data from the telemetry stream without modification, allowing access to the individual data points. For the science data, an IDL computer program, produced automatically by a translator application from LASP that uses a telemetry-definitions database as its input, decommutates individual telemetry items from science packets. Time conversions from the Mission Elapsed Time (MET) in packet headers to TAI and UTC are done using SPICE, via the ICY IDL interface. The output of this step is stored in an IDL save file in the form of an IDL structure with appropriate time tags.

The second task of the L0 to L1 processing step is to convert the L0 science data into L1 data. For this step, another IDL computer program from LASP receives the IDL save file containing the L0 data and then converts the L0 data into L1 data. The L1 data are stored in a Common Data Format (CDF) file at the SOC for public access. (As the data are specific

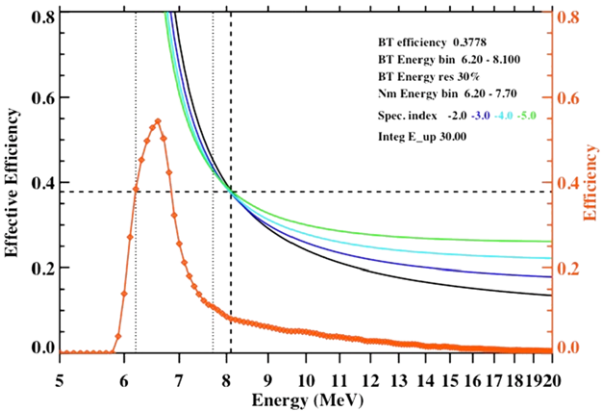

Fig. 27 Bow tie efficiency derived from the full efficiency for the 6.2–7.7 MeV electron differential energy channel

to the instrument, the CDF file does not meet the requirements of the Standard file format guidelines of the COSPAR Panel on Radiation Belt Environment.)

The final task of the L0 to L1 processing step is to re-assemble the daily MET L1 files produced into daily UTC files. This is a processing step that uses a generic process for this task developed at the ECT SOC (since all the ECT instrument L1 data files needed to undergo this step). During this step the ECT SOC also checks, and if necessary, corrects all the MET → UTC time conversions done to enforce consistency in this process across all ECT data products.

After this, the L1 data are converted into Level 2 (L2) data, the first level of useable science data. Codes for the L1 → L2 process are provided by LASP and run at the LANL ECT SOC as part of the ECT data processing chain. The measure count rates are corrected for background and dead time effects. The corrected count rate data are converted to physical flux units (i.e., cm^2 sr s MeV). The conversion from count rates to flux will be a two-step process; in the first step the differential channel efficiencies will be approximated using a bow-tie analysis (Van Allen et al. 1974), which simplifies the energy dependence of the efficiencies to a constant value over an energy range. Figure 27 shows the efficiency as a function of incident electron energy and the corresponding bow tie approximated result for the nominal 6.2–7.7 MeV channel. From the figure it can be seen that the full efficiency can be approximated as a constant of ∼0.38 over an energy range of 6.2–8.1 MeV. Table 7 lists the bow tie efficiencies and the energy bin widths for all the electron differential channels. As mentioned earlier, the full efficiency curves are obtained through logic equations that are software commandable and correspondingly bow tie values can be obtained when the logic conditions are changed. To compute the flux determination, the electron spectrum obtained from the bow tie fluxes is used as the input spectrum for an iterative minimization procedure, which uses the full efficiencies to obtain the final fluxes and spectrum.

The procedure is much more straightforward for protons as the full efficiencies for protons are already in the form of a constant value over each energy bin.

The Level 2 output will be saved in a CDF file meeting the PRBEM (Panel on Radiation Belt Environment) standard format guidelines. The data levels higher than Level 2 will combine the data from other RBSP instruments, e.g., local magnetic field direction in order to obtain pitch angles, and will be stored in PRBEM CDF format.

All higher-level data processing beyond L1 will take place at the ECT SOC using a common set of utilities and codes, since all ECT instrument data in L2 format have a high degree of commonality (count rates per detector, spin sector and energy).

Table 7 Electron channel efficiencies and bin widths derived from logic equation efficiencies through bow tie analysis

Electron channel No.	Nominal energy	Bow tie energy	Bow tie efficiency	Bow tie bin width	Bow tie bin center
0	1.6–2.0	1.6–3.0[a]	0.028	1.4	2.30
1	2.0–2.5	2.0–2.6	0.199	0.6	2.30
2	2.5–3.2	2.5–3.2	0.503	0.7	2.85
3	3.2–4.0	3.2–4.0	0.348	0.8	3.60
4	4.0–5.0	4.0–5.0	0.574	1.0	4.50
5	5.0–6.2	5.0–6.2	0.445	1.2	5.60
6	6.2–7.7	6.2–8.1	0.378	1.9	7.15
7	7.7–9.7	7.7–9.9	0.265	2.2	8.80
8	9.7–12.1	9.7–13.6	0.132	3.9	11.65
9	12.1–15.1	12.1–18.6	0.078	6.5	15.35
10	15.1–18.9	15.1–30.0	0.036	14.9	22.55
11	>18.9	18.9–100	0.001	81.1	59.45

[a]Preliminary value

As alluded to previously, the processing of REPT telemetry data will occur in parallel both at the LANL SOC and LASP. During flight, LASP will pull recent, downlinked packet files from the SOC to determine instrument health and the quality of science data. The processing at LASP decommutates housekeeping and science data from packet files and ingests it into a database. Individual data points are then accessible to various standard LASP analysis tools. These tools produce line plots and color-coded limits information for health and safety checking. (The code leverages generic libraries used on many other LASP missions.) If needed, the processing code will be updated to provide new calibrations and corrections. The new versions of the processing codes are kept in sync between LASP and the SOC so that both are always running the same version.

The L2 data are suitable for scientific analyses, such as the characterization of spectral variability, or whether spectra harden during energization events. The data are also useful for synoptic views of the radiation belts such as seen in Fig. 1. Studies of changes in angular distributions of particle flux are also amenable to L2 data, although knowledge of pitch angle requires the sector fluxes be mapped to B field. The Level 3 data incorporates the geomagnetic field direction and thus provide the pitch angle information. Characterization of pitch angle distributions will enable answering key issues in electron energization, such as whether energization and isotropization are nearly simultaneous; energization models have differing predictions regarding evolution of pitch angle distributions and therefore be used to identify the particular mechanism. The highest-level data, Level 4, will combine measurements with global magnetic field models to produce phase space densities. As mentioned before (see Fig. 4) the radial gradient of PSD is the chief discriminator for distinguishing transport vs. in-situ energization of electrons. REPT measurements of PSD then, together with plasma wave data from other RBSP instruments, provide a complete picture of energization and loss mechanisms of relativistic electrons, which is a key goal of the RBSP mission.

6 Discussion and Summary

This paper has provided a comprehensive description of the physical design, engineering characteristics, laboratory calibrations, and expected scientific contributions of the Relativistic Electron-Proton Telescope instruments that are a key part of the scientific payload onboard the RBSP dual-spacecraft mission. As has been detailed in this paper, measurements of the electrons in the energy range $E \sim 1$ MeV to $E \sim 20$ MeV throughout the outer and inner Van Allen belts are absolutely central to the mission objectives of the RBSP program. Careful design efforts based on prior mission heritage (CRRES, SAMPEX, and POLAR) and effective use of the GEANT4 instrument simulation tools have allowed achievement of superior REPT performance properties while using only modest spacecraft resources. Laboratory characterization and high-energy accelerator calibrations have shown that the REPT flight instruments are closely identical to one another and they also have the key performance characteristics that have been demanded by the RBSP mission Level 1 requirements.

The REPT instruments will work in close harmony with the other sensors that make up the overall RBSP scientific payload. While there is some energy overlap of REPT with other particle detectors (e.g., MagEIS and RPS), the REPT measurements will be unique for electrons in the several MeV energy range (and above) and for protons in the 20–50 MeV energy range. These particles are, respectively, of key importance in the outer Van Allen zone and inner Van Allen belt. It is important to always recall that the RBSP mission is a flagship component of the NASA Living With a Star program. As such, it is crucial to complete our understanding of how our active Sun distorts and stresses the near-Earth environs in ways that can efficiently and effectively accelerate charged particles to the immense energies that REPT will observe.

REPT will utilize concurrent magnetic field and plasma wave observations to address long-standing puzzles about the cosmic particle accelerator that operates so remarkably in Earth's magnetosphere. While there will be fascinating scientific studies of low-energy particle processes and wave phenomena using the capable RBSP payload, the central goal of the program is to provide definitive understanding of the highest energy proc-esses. As such, it is clearly the goal of our investigation to look carefully at the connected Sun-Earth system and use the most powerful space weather disturbances to develop effective, predictive models of the magnetospheric response. Our data analysis, visualization tools, and information dissemination methods are all geared toward rapid and efficient infusion of knowledge into our national space weather and LWS systems.

It is both remarkable and sobering that over five decades have passed since the discovery of the Earth's radiation belts by Van Allen and co-workers. With the development, integration, testing and operation of the RBSP mission elements, the space physics community will at long last have the requisite tools to understand the complexities of radiation belt dynamics. It will be a fitting tribute to the pioneering spirit of J.A. Van Allen to return to this first discovery of the Space Age and to address in depth the mysteries of cosmic particle energization.

Acknowledgements We want to express our sincere appreciation to all of our colleagues at the Laboratory for Atmospheric and Space Physics for their support in the successful completion of the REPT instrument. We thank our RBSP and ECT teammates for their assistance, especially J. Bernard Blake, Joseph F. Fennell, Bill Crain, Joseph E. Mazur, John Goldsten, Brian Klatt, and Jim Cravens. We also want to thank the APL payload, spacecraft and mission teams, specifically Lori Suther, Al Reiter, Elliot Rodberg, and Annette Dolbow.

Special thanks to all of the reviewers who contributed their expertise to the improvement of our instrument. In particular we are grateful to Berndt Klecker, Richard Mewaldt, Edward S. Stone, Tycho Von Rosenvinge, Frank B. McDonald, Gary Mullen, Bronislaw Dichter, Gary Galica, Gregory Ginet, and Steve Battel.

This work has been supported by NASA prime contract NAS5-01072 to Johns Hopkins University Applied Physics Laboratory (JHU/APL).

References

M.H. Acuña et al., in *The Global Geospace Mission*, ed. by C.T. Russell (Kluwer Academic, Dordrecht, 1996)

J. Alcaraz et al., Cosmic protons. Phys. Lett. B **490**, 27–35 (2000)

S. Agostinelli et al., Nuclear instruments and methods in physics research section A: accelerators, spectrometers, detectors and associated equipment. Nucl. Instrum. Methods A **506**, 250–303 (2003). doi:10.1016/S0168-9002(03)01368-8

C.A.J. Ammerlaan, R.F. Rumphorst, L.A.Ch. Koerts, Particle identification by pulse shape discrimination in the p-I-n type semiconductor detector. Nucl. Instrum. Methods **22**, 189–200 (1963)

D.N. Baker, P.R. Higbie, R.D. Belian, E.W. Hones Jr., Do Jovian electrons influence the terrestrial outer radiation zone? Geophys. Res. Lett. **6**(6), 531–534 (1979). doi:10.1029/GL006i006p00531

D.N. Baker et al., The Los Alamos geostationary orbit synoptic data set: a compilation of energetic particle data. Los Alamos National Laboratory Report, LA-8843, 1981

D.N. Baker et al., Highly relativistic magnetospheric electrons: a role in coupling to the middle atmosphere? Geophys. Res. Lett. **14**(10), 1027–1030 (1987). doi:10.1029/GL014i010p01027

D.N. Baker, R.L. McPherron, T.E. Cayton, R.W. Klebesadel, Linear prediction filter analysis of relativistic electron properties at $6.6R_E$. J. Geophys. Res. **95**, 15,133–15,140 (1990). doi:10.1029/JA095iA09p15133

D.N. Baker, G.M. Mason, O. Figueroa, G. Colon, J. Watzin, R. Aleman, An overview of the SAMPEX mission. IEEE Trans. Geosci. Electron. **31**, 531 (1993)

D.N. Baker, J.B. Blake, L.B. Callis, J.R. Cummings, D. Hovestadt, S. Kanekal, B. Klecker, R.A. Mewaldt, R.D. Zwickl, Relativistic electron acceleration and decay time scales in the inner and outer radiation belts: SAMPEX. Geophys. Res. Lett. **21**, 409 (1994)

D.N. Baker et al., A strong CME-related magnetic cloud interaction with the earth's magnetosphere: ISTP observation of rapid relativistic electron acceleration on May 15, 1997. Geophys. Res. Lett. **25**(15), 2975–2978 (1998). doi:10.1029/98GL01134

D.N. Baker et al., An extreme distortion of the Van Allen belt arising from the 'Hallowe'en' solar storm in 2003. Nature **432**, 878–881 (2004). doi:10.1038/nature03116

D.N. Baker et al., Low-altitude measurements of 2–6 MeV electron trapping lifetimes at $1.5 \leq l \leq 2.5$. Geophys. Res. Lett. **34**, L20110 (2007). doi:10.1029/2007GL03100

D.N. Baker, D. Mitchell, P. O'Brien, RBSP project internal report. JHUAPL, 2008

J.-F. Beche, Second order pseudo-Gaussian shaper. Lawrence Berkeley National Laboratory. LBNL Paper LBNL-52855, 2002

J.B. Blake, W.A. Kolasinski, R.W. Fillius, E.G. Mullen, Injection of electrons and protons with energies of tens of MeV into $L < 3$ on 24 March 1991. Geophys. Res. Lett. **19**(8), 821–824 (1992). doi:10.1029/92GL00624

J.B. Blake et al., The MagEIS/ECT instrument on the RBSP mission. Space. Sci. Rev. (2012, this issue)

J. Bortnik et al., An observation linking the origin of plasmaspheric hiss to discrete chorus emissions. Science **324**, 5928 (2009)

W.R. Cook et al., PET: a proton/electron telescope for studies of magnetospheric, solar, and galactic particles. IEEE Trans. Geosci. Electron. **31**, 565 (1993)

S.R. Elkington, M.K. Hudson, A.A. Chan, Acceleration of relativistic electrons via drift-resonant interaction with toroidal-mod Pc-5 ULF oscillations. Geophys. Res. Lett. **26**(21), 3273 (1999)

S.R. Elkington, M.K. Hudson, A.A. Chan, Resonant acceleration and diffusion of outer zone electrons in an asymmetric geomagnetic field. J. Geophys. Res. **108**(A3), 1116 (2003)

S.R. Elkington, M. Wiltberger, A.A. Chan, D.N. Baker, Physical models of the geospace radiation environment. J. Atmos. Sol.-Terr. Phys. **66**, 1371 (2004)

S.R. Elkington, D.N. Baker, M. Wiltberger, in *The Inner Magnetosphere: Physics and Modeling*, ed. by T.I. Pulkkinen, N.A. Tsyganenko, R.H.W. Friedel. AGU Geophysical Monograph, vol. 155 (American Geophysical Union, Washington, 2005), p. 147

T.I. Gombosi, G. Toth, D.L. de Zeeuw, K.C. Hansen, K. Kabin, K.G. Powell, Semirelativistic magnetohydrodynamics and physics-based convergence acceleration. J. Comput. Sci. **177**, 176 (2002)

M.G. Gornov et al., Selection of the shaping circuits of a multilayer semiconductor spectrometer of charged particles. Instrum. Exp. Tech. **45**(5), 626–630 (2002)

J.C. Green, M.G. Kivelson, Relativistic electrons in the outer radiation belt: differentiating between acceleration mechanisms. J. Geophys. Res. **109**, A03213 (2004). doi:10.1029/2003JA010153
R.B. Horne, R.M. Thorne, Potential waves for relativistic electron scattering and stochastic acceleration during magnetic storms. Geophys. Res. Lett. **25**(15), 3011–3014 (1998). doi:10.1029/98GL01002
R.B. Horne, N.P. Meredith, R.M. Thorne, D. Heynderickx, R.H.A. Iles, R.R. Anderson, Evolution of energetic electron pitch angle distributions during storm time electron acceleration to megaelectronvolt energies. J. Geophys. Res. **108**(A1), 1016 (2003). doi:10.1029/2001JA009165
R.B. Horne, D.N. Baker et al., Wave acceleration of electrons in the Van Allen radiation belts. Nature **437**, 227–230 (2005a). doi:10.1038/nature03939
R.B. Horne, R.M. Thorne, S.A. Glauert, J.M. Albert, N.P. Meredith, R.R. Anderson, Timescale for radiation belt electron acceleration by whistler mode chorus waves. J. Geophys. Res. **110**, A03225 (2005b). doi:10.1029/2004JA010811
M.H. Johnson, J. Kierein, Combined release and radiation effects satellite (CRRES): spacecraft and mission. J. Spacecr. Rockets **29**(4), 556–563 (1992). doi:10.2514/3.55641
S.G. Kanekal et al., Magnetospheric response to magnetic cloud (coronal mass ejection) events: relativistic electron observations from SAMPEX and polar. J. Geophys. Res. **104**, A11 (1999). doi:10.1029/1999JA900239
C.A. Kletzing et al., The electric and magnetic field instrument suite and integrated science (EMFISIS) on RBSP. Space. Sci. Rev. (2012, this issue)
L.J. Lanzerotti et al., Radiation belt storm probes ion composition experiment (RBSPICE). Space Sci. Rev. (2012, this issue)
C. Leroy et al., Study of charge transport in non-irradiated and irradiated silicon detectors. Nucl. Instrum. Methods Phys. Res. **A426.1**, 99–108 (1999)
X. Li et al., Simulation of dispersionless injections and drift echoes of energetic electrons associated with substorms. Geophys. Res. Lett. **25**, 3763 (1998)
X. Li et al., Quantitative prediction of radiation belt electrons at geostationary orbit based on solar wind measurements. Geophys. Res. Lett. **28**(9), 1887–1890 (2001a). doi:10.1029/2000GL012681
X. Li et al., Long term measurements of radiation belts by SAMPEX and their variations. Geophys. Res. Lett. **28**(20), 3827–3830 (2001b). doi:10.1029/2001GL013586
B.W. Loo, F.S. Goulding, D. Gao, Ballistic deficits in pulse shaping amplifiers. IEEE Trans. Nucl. Sci. **35.1**, 114–118 (1988)
K.R. Lorentzen et al., Multisatellite observations of MeV ion injections during storms. J. Geophys. Res. **107**(A9), 1231 (2002). doi:10.1029/2001JA000276
J.G. Lyon, J.A. Fedder, C.M. Mobarry, The Lyon-Fedder-Mobarry global MHD magnetospheric simulation code. J. Atmos. Sol.-Terr. Phys. **66**(15), 1333 (2004)
J.P. McCollough et al., Physical mechanisms of compressional EMIC wave growth. J. Geophys. Res. **115**, A10214 (2010)
B.H. Mauk et al., Science objectives and rational for the Radiation Belt Storm Probes Mission. Space Sci. Rev. (2012). doi:10.1007/s11214-012-9908-y
J.E. Mazur et al., The Relativistic-Proton Spectrometer (RPS) for the Radiation Belt Storm Probes Mission. Space Sci. Rev. (2012). doi:10.1007/s11214-012-9926-9
R.A. Mewaldt, Solar energetic particle composition, energy spectra, and space weather. Space Sci. Rev. **124**, 303–316 (2006). doi:10.1007/s11214-006-909-0
N.P. Meredith et al., Evidence for chorus-driven electron acceleration to relativistic energies from a survey of geomagnetically disturbed periods. J. Geophys. Res. **108**(A6), 1248 (2003). doi:10.1029/2002JA009764
C.H. Mosher, Pseudo-Gaussian transfer functions with superlative baseline recovery. IEEE Trans. Nucl. Sci. **23**(1), 226–228 (1976)
G.A. Paulikas, J.B. Blake, Effects of the solar wind on magnetospheric dynamics: energetic electrons at the synchronous orbit, in *Quantitative Modeling of Magnetospheric Processes*, ed. by W.P. Olson. Geophys. Monogr. Ser., vol. 21 (AGU, Washington, 1979), pp. 180–202
J. Raeder, Global magnetohydrodynamics, a tutorial, in *Space Plasma Simulation*, ed. by C.T. Dum, M. Scholer, J. Buchner. Lecture Notes in Physics, vol. 615 (Springer, New York, 2003), p. 212
J.G. Roederer, *Dynamics of Geomagnetically Trapped Radiation* (Springer, New York, 1970)
I. Roth, M. Temerin, M.K. Hudson, Resonant enhancement of relativistic electron fluxes during geomagnetically active periods. Ann. Geophys. **17**, 631 (1999)
T.E. Sarris, X. Li, N. Tsaggas, N. Paschalidis, Modeling energetic particle injections in dynamic pulse fields with varying propagation speeds. J. Geophys. Res. **107**(A3), 1033 (2002)
Y.Y. Shprits et al., Outward radial diffusion driven by losses at the magnetopause. J. Geophys. Res. **111**, A11214 (2006)
H.E. Spence et al., The ECT investigation on the RBSP mission. Space Sci. Rev. (2012, this issue)

P.A. Sturrock, *Plasma Physics* (Cambridge University Press, Cambridge, 1994)
M.G.G.T. Taylor, R.H.W. Friedel, G.D. Reeves, M.W. Dunlop, T.A. Fritz, P.W. Daly, A. Balogh, Multisatellite measurements of electron phase space density gradients in Earth's inner and outer magnetosphere. J. Geophys. Res. **109**, A05220 (2004)
A.L. Vampola, Measuring energetic electrons—what works and what doesn't, in *Measurement Techniques in Space Plasmas: Particles*, ed. by F. Pfaff, E. Borovsky, T. Young. Geophys. Monogr. Ser., vol. 102 (AGU, Washington, 1998), pp. 339–355. doi:10.1029/GM102p0339
J.A. Van Allen et al., Energetic electrons in the magnetosphere of Jupiter. Science **183**, 309 (1974)
J. Vette, The NASA/National Space Science Data Center trapped radiation environment model program (1964–1991). NSSDC Report 91-29, Greenbelt, MD, 1991
J. Wygant et al., The EFW investigation and instruments on the RBSP mission. Space. Sci. Rev. (2012, this issue)